Inverse modeling estimates of the global nitrous oxide surface flux from 1998–2001

A. I. Hirsch,[1,2] A. M. Michalak,[3] L. M. Bruhwiler,[1] W. Peters,[1,2]
E. J. Dlugokencky,[1] and P. P. Tans[1]

Received 29 December 2004; revised 24 October 2005; accepted 10 November 2005; published 11 February 2006.

[1] Measurements of nitrous oxide in air samples from 48 sites in the Cooperative Global Air Sampling Network made by NOAA/ESRL GMD CCGG (the Carbon Cycle Greenhouse Gases group in the Global Monitoring Division at the NOAA Earth System Research Laboratory in Boulder, Colorado) and the three-dimensional chemical transport model TM3 were used to infer global nitrous oxide fluxes and their uncertainties from 1998–2001. Results are presented for four semihemispherical regions (90°S–30°S, 30°S to equator, equator to 30°N, 30°N–90°N) and six broad "super regions" (Southern Land, Southern Oceans, Tropical Land, Tropical Oceans, Northern Land, and Northern Oceans). We found that compared to our a priori estimate (from the International Geosphere-Biosphere Programme's Global Emissions Inventory Activity), the a posteriori flux was much lower from 90°S–30°S and substantially higher from equator to 30°N. Consistent with these results, the a posteriori flux from the Southern Oceans region was lower than the a priori estimate, while Tropical Land and Tropical Ocean estimates were higher. The ratio of Northern Hemisphere to Southern Hemisphere fluxes was found to range from 1.9 to 5.2 (depending on the model setup), which is higher than the a priori ratio (1.5) and at the high end of previous estimates. Globally, ocean emissions contributed 26–36% of the total flux (again depending on the model setup), consistent with the a priori estimate (29%), though somewhat higher than some other previous estimates.

Citation: Hirsch, A. I., A. M. Michalak, L. M. Bruhwiler, W. Peters, E. J. Dlugokencky, and P. P. Tans (2006), Inverse modeling estimates of the global nitrous oxide surface flux from 1998–2001, *Global Biogeochem. Cycles*, *20*, GB1008, doi:10.1029/2004GB002443.

1. Introduction

[2] The continuing increase of the global atmospheric nitrous oxide burden is of concern for two main reasons: N_2O's potency as an infrared radiation absorber and its role in modulating the stratospheric ozone layer. N_2O has a greenhouse warming potential of almost 300 relative to CO_2 over a 100-year time horizon [*Prather and Ehhalt*, 2001] and is one of the six main greenhouse gases covered by the United Nations Framework Convention on Climate Change (UNFCCC) and the Kyoto Protocol. This importance on a per mass basis is tempered by a much smaller increase relative to CO_2 since the preindustrial era. These two factors combine to give a radiative forcing of N_2O due to its increase over preindustrial levels of 0.15 W m^{-2} in 2001 [*Prather and Ehhalt*, 2001], or 10% of the CO_2 radiative forcing. Nitrous oxide's importance in ozone chemistry derives from the fact that 6% of the N_2O loss in the stratosphere is due to reaction with excited oxygen atoms through a pathway that produces nitric oxide. This nitric oxide is introduced in the midstratosphere, where it participates in a catalytic cycle that destroys ozone [*Crutzen*, 1974; *Nevison and Holland*, 1997].

[3] Over the past 2 decades, as measurements have become more precise and widespread, the details of the global nitrous oxide budget have started to emerge. On a global scale, the atmospheric increase of nitrous oxide is currently 0.2 to 0.3% per year [*Zander et al.*, 1994; *Prinn et al.*, 1998, 2000; *Prather and Ehhalt*, 2001]. NOAA/ESRL measurements show a trend of 0.73 ± 0.06 ppb per year for 1999–2001 [*Hall et al.*, 2002], equal to about 3.5 MtN yr^{-1} (1 MtN = 1 × 10^{12} gN). We have better knowledge of N_2O's atmospheric lifetime, now thought to be 122 ± 24 years, based on stratospheric measurements [*Volk et al.*, 1997]. This measurement-based estimate of the lifetime is consistent with theoretical estimates [*Prinn et al.*, 1998; *Minschwaner et al.*, 1993]. Dividing the present atmo-

[1]Global Monitoring Division, Earth System Research Laboratory, National Oceanic and Atmospheric Administration, Boulder, Colorado, USA.
[2]Also at Cooperative Institute for Research in Environmental Sciences, University of Colorado, Boulder, Colorado, USA.
[3]Department of Civil and Environmental Engineering, University of Michigan, Ann Arbor, Michigan, USA.

0886-6236/06/2004GB002443$12.00

spheric content of N_2O by the best estimate of the lifetime yields a stratospheric loss of about 12.5 ± 2.5 MtN yr^{-1}. Therefore we can estimate the net source from the surface to be ~16 MtN yr^{-1} by adding the stratospheric loss and the atmospheric increase. With the assumption that atmospheric nitrous oxide was in steady state during the preindustrial era, we can also estimate the degree to which industrial society has tipped the nitrous oxide budget out of balance. A preindustrial global average concentration of 265–280 ppb [*Machida et al.*, 1995; *Flückiger et al.*, 2002; *Battle et al.*, 1996] and the same lifetime of 122 years yield a preindustrial source of 10.4–11.0 MtN yr^{-1}. In other words, human activities have increased the annual source of nitrous oxide from the surface of the Earth by about 40–50% over preindustrial levels, assuming that natural sources and the stratospheric lifetime have not changed. Isotopic measurements made on polar firn air suggest that the anthropogenic N_2O source has been dominated by agricultural emissions [*Rahn and Wahlen*, 2000; *Röckmann et al.*, 2002].

[4] While net surface sinks for nitrous oxide have been measured in some instances, such as anoxic ocean waters and sediments [*Cohen*, 1978; *Elkins et al.*, 1978], grasslands [*Blackmer and Bremer*, 1976; *Brice et al.*, 1977; *Ryden*, 1981], hot and dry savanna soils [*Donoso et al.*, 1993], midlatitude forests [*Castro et al.*, 1992] and treed boreal bogs [*Schiller and Hastie*, 1994], it is not known to what degree these sinks affect the global budget. Chemical production and destruction of nitrous oxide in the free atmosphere at altitudes below about 50 hPa (~22 km) is thought to be small, with the possible exception of formation in power plant plumes. However, high estimates of N_2O production by power plants, once thought to dominate the budget [*Weiss and Craig*, 1976; *Pierotti and Rasmussen*, 1976; *Hao et al.*, 1987], were the result of a measurement artifact [*Muzio and Kramlich*, 1988]. Several smaller sources, including biomass burning, sewage, nitrogen fertilizers, nylon manufacture, automobiles, and others were thought to add up to the required amount to balance the budget once the power plant source was removed [*Khalil and Rasmussen*, 1992; *Kroeze et al.*, 1999]. *Nevison and Holland* [1997] include a more complete history of efforts to understand the global N_2O budget and to quantify its atmospheric lifetime. A global, gridded inventory has recently been assembled that contains a current understanding of the geographic distribution of surface nitrous oxide sources [*Bouwman et al.*, 1995]. However, the source magnitudes are uncertain and little is known about the seasonality of surface sources or sinks [*Bouwman and Taylor*, 1996].

[5] Inverse modeling presents a method to reduce the present uncertainties in the global budgets of atmospheric trace species and also provides a way to test whether inventory estimates are consistent with the atmospheric record. To date, inverse modeling studies have quantified global scale sources for many radiatively and chemically important trace gases such as CFCs [*Brown*, 1993; *Hartley and Prinn*, 1993; *Plumb and Zheng*, 1996; *Mulquiney and Norton*, 1998; *Mulquiney et al.*, 1998], CH_4 [*Brown*, 1993, 1995; *Hein et al.*, 1997; *Houweling et al.*, 1999], CO_2 [*Tans et al.*, 1990; *Bousquet et al.*, 1996; *Law and Simmonds*, 1996; *Enting et al.*, 1995; *Kaminski et al.*, 1999; *Fan et al.*, 1998; *Bousquet et al.*, 2000; *Gurney et al.*, 2002; *Rödenbeck et al.*, 2003], and most relevant to this study, N_2O [*Prinn et al.*, 1990]. Nitrous oxide, while featuring high greenhouse warming and ozone depleting potentials, presents some challenges to continental scale global inverse modeling efforts. Despite the excellent precision of the measurements (~0.2 ppb, or 0.07%), the signal-to-noise ratio is still fairly low for most features in the N_2O record such as the seasonal cycle since they are small relative to the background concentration. For example, the amplitude of the seasonal cycle at Mace Head Ireland is on the order of 0.1% of the mean concentration [*Prinn et al.*, 2000; *Liao et al.*, 2004; *Nevison et al.*, 2004]. Also, stratospheric photochemical loss is a major term in the N_2O budget, whose impact on surface measurements must be accounted for in the inversion so that it is not interpreted as a surface flux signal. This complication is not present for CO_2.

[6] The largest signal in tropospheric N_2O is the north-south interhemispheric difference of roughly 0.7–1 ppb [*Butler et al.*, 1989; *Cicerone*, 1989; *Prinn et al.*, 1990, 2000; *Prather and Ehhalt*, 2001; *Hall et al.*, 2002]. This feature has been explored with box models, ranging from two to 12 boxes (four in the lower troposphere, four in the upper troposphere and four in the stratosphere, all zonally averaged). These models have used the interhemispheric gradient to estimate the ratio of Northern to Southern Hemisphere sources as ranging from 1.5 to 2.0 [*Butler et al.*, 1989; *Cicerone*, 1989; *Prinn et al.*, 1990, 2000]. The twelve-box study [*Prinn et al.*, 1990] used data from an expanded network of high-precision measurements (five stations distributed from 41°S to 53°N, with measurements made 12 times per day) called the Atmospheric Lifetime Experiment–Global Atmospheric Gases Experiment (ALE-GAGE) to infer surface fluxes for four semihemispherical basis regions for the 1980s. That study suggested that the atmospheric measurements were not consistent with power plants being a large source of N_2O. Rather, tropical forest disturbance and midlatitude fertilizer use were cited for the imbalance in the nitrous oxide budget. The work presented here is one of the first attempts at the inverse problem for N_2O since the *Prinn et al.* [1990] study and the first to employ a 3-D Chemical Transport Model (CTM) for that purpose.

[7] Today, the measurement network for nitrous oxide has expanded even further. High precision measurements of nitrous oxide in the NOAA Earth Systems Research Laboratory Global Monitoring Division (NOAA/ESRL GMD, formerly NOAA/CMDL) Carbon Cycle Greenhouse Gases (CCGG) group Cooperative Global Air Sampling Network flask samples began in June of 1997 and today include measurements at over 50 sites, including high-altitude sites and vertical profiles using aircraft. Figure 1 is a smoothed and interpolated surface constructed from measurements made by the NOAA/ESRL GMD CCGG group on flasks filled in the marine boundary layer, provided to help visualize the global scale general spatial and temporal patterns. The globally averaged concentration has both

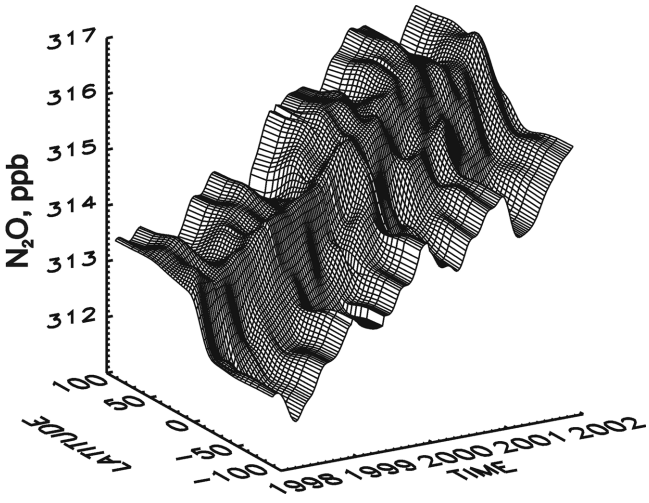

Figure 1. Latitude-time surface of smoothed and interpolated N_2O in the marine boundary layer from the beginning of 1998 through the end of 2001.

seasonal and interannual variability in its growth rate. The latitudinal gradient shows interannual variability, suggesting that the north-south ratio of fluxes or interhemispheric transport varies from year to year. The high precision of N_2O measurements has also allowed diagnosis of the N_2O seasonal cycle [*Prinn et al.*, 2000; *Liao et al.*, 2004; *Nevison et al.*, 2004], with an amplitude of about 0.4 ppb in the Northern Hemisphere and 0.3 ppb in the Southern Hemisphere. Interestingly, the seasonal cycles in the two hemispheres are not exactly 6 months out of phase. The seasonal cycle may be due in part to seasonal variability in surface fluxes. It may also be due to seasonal transport changes, either within the troposphere or in stratosphere-troposphere exchange (STE), which delivers N_2O-poor stratospheric air to the troposphere [*Nevison et al.*, 2004; *Morgan et al.*, 2004]. Inverse modeling can help quantify the relative contributions of these different processes in order to extract information about the surface flux, which was the quantity of interest in this study.

[8] This study had two aims: (1) explore to what degree the NOAA/ESRL GMD CCGG group Cooperative Global Air Sampling Network data could be used to constrain the global budget of nitrous oxide with higher spatial resolution than has been attempted to this point, and (2) diagnose whether the geographical distribution of the global nitrous oxide surface source has changed since the 1980s. To address these two aims, we divided the Earth's surface in two different ways, and solved for the surface N_2O flux for the resulting regions (commonly called basis regions). First, for comparison with the *Prinn et al.* [1990] study, we divided the world into four equal-area semihemispherical basis regions, with no division between land and ocean. To see whether fluxes using a finer geographical division could be constrained by the measurement network, we used the 22 continental scale TransCom3 basis regions [see *Gurney et al.*, 2002] and aggregated the results after the inversion into six broad super regions after performing the inversion. Multiyear (1998–2001) average results are presented for the four semihemispherical basis function case and for the six TransCom3 super regions.

2. Methodology

[9] This study used Bayesian Synthesis inverse modeling which solves for the entire time series of the total surface N_2O flux for all regions at once. In this approach, the monthly averaged N_2O concentrations at different points on the globe (48 of the NOAA/ESRL GMD CCGG Cooperative Global Air Sampling Network sites) are modeled as the linear combination of the influence of fluxes from the geographical basis regions for which we are estimating the flux. The influence of N_2O emissions from a given geographical region on a measurement at a given location is simulated with a chemical transport model (CTM). For this purpose, we used the Transport Model 3 (TM3 [*Heimann*, 1995; *Heimann and Körner*, 2003]) with analyzed winds and mixing parameters from the National Center for Environmental Prediction (NCEP). The inversion begins with an initial a priori estimate of the fluxes (the GEIA inventory). These fluxes are adjusted such that the variance is minimized (in a least squares sense) between the new flux estimates and the a priori fluxes and between modeled concentrations (using the a posteriori fluxes) and the measured concentrations (the NOAA flask measurements).

2.1. Basis Regions

[10] We present multiyear average fluxes for the four semihemisphere basis regions, and for the six TransCom3 super regions. The semihemispherical basis regions break the globe into four equal-area regions (90°S–30°S, 30°S to equator, equator to 30°N, 30°N–90°N), without distinction between land and ocean. As stated above, the TransCom3 setup used the 22 continental scale TransCom3 basis regions for the inversion, with results aggregated after the inversion into the same larger super regions used by *Gurney et al.* [2002]. This aggregation allowed us to take advantage of the error reduction that results from anticorrelations between different regions that are not well resolved from each other by the inverse model. In other words, the inversion was performed using 22 regions and monthly resolution and the Green's function matrix had a separate column for each region in each month; after the inversion, the a posteriori fluxes were aggregated into the super regions and both the diagonal and off-diagonal elements of the a posteriori flux covariance matrix were summed for each super region to give the variance of the a posteriori fluxes. We show all 22 TransCom3 regions in Figure 2 to illustrate the composition of the aggregated super regions, though we do not present results for the individual TransCom3 regions. The super regions are as follows: Northern Land = boreal North America (region 1 in Figure 2), boreal Asia (7), temperate North America (2), Europe (11), and Central Asia (8); Tropical Land = tropical South America (3), North Africa (5), and South East Asia (9); Southern Land = temperate South America (4), southern Africa (6), and Australia/New Zealand (10); Northern Oceans = Arctic Ocean (16), north Atlantic (17), north Pacific (12); Tropical Oceans = tropical Atlantic (18), eastern tropical Pacific (14), western tropical Pacific (13), and northern Indian (21);

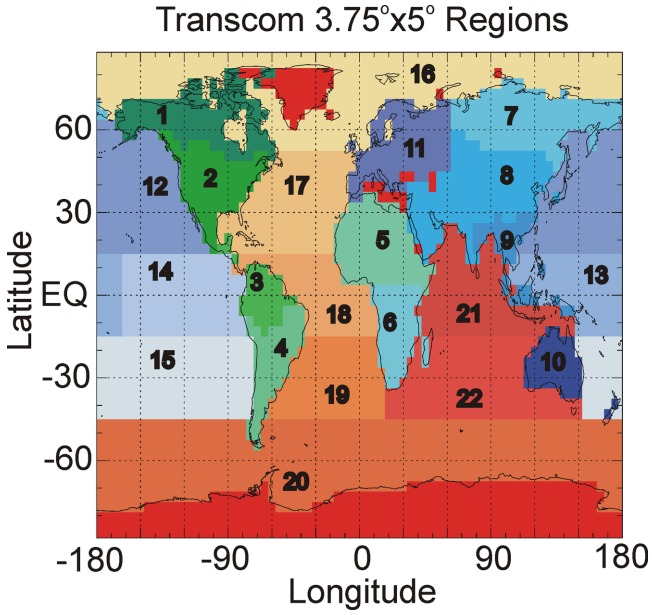

Figure 2. The 22 TransCom3 regions. Greenland and Antarctica were assumed to have zero flux in this study. These continental scale regions were aggregated after the inversion into six super regions, as described in the text. Only the results for the super regions are presented in this study.

Southern Oceans = the southern Atlantic (19), southern Pacific (15), south Indian (22), and the Southern Ocean (20). Antarctica and Greenland were assumed to have zero surface flux in this study. We used the flux basis regions defined by the TransCom3 project for two reasons. First, the regions correspond fairly well to areas of biological interest, such as the ocean gyres, areas of ocean upwelling, and terrestrial biomes. Second, this choice allows comparison of the fluxes of CO_2 and N_2O on the same geographical basis, to look for similarities or differences in the forces that drive the net fluxes of the two species (for example, biomass burning or ocean upwelling), though no such comparisons were performed in this study.

2.2. NOAA/ESRL GMD CCGG Cooperative Global Air Sampling Network

[11] N_2O data used in the inverse modeling are from surface air samples collected as part of the NOAA/ESRL GMD CCGG Cooperative Global Air Sampling Network. Surface samples are collected in duplicate, approximately weekly, from a globally distributed network of background air sampling sites [*Dlugokencky et al.*, 1994]. N_2O dry-air mole fractions (nmol mol^{-1}, abbreviated ppb) are determined at NOAA/ESRL GMD in Boulder, Colorado, USA, by gas chromatography with electron capture detection (ECD). Chromatographic methods are as in the work of *Butler et al.* [1989]. The normalized ECD response for N_2O is determined monthly using six gravimetrically prepared standards [*Hall et al.*, 2002] covering the nominal range 240 to 345 ppb. N_2O chromatographic peaks in air samples are normalized to the same cylinder of natural air (reference gas) that is used to determine the monthly normalized instrument response curves. Each aliquot of sample is bracketed by aliquots of air from the reference cylinder; repeatability of the analytical system, determined as one standard deviation of multiple measurements of air from a cylinder containing natural air, is 0.2 ppb. The standard deviation of the absolute value of the difference between members of pairs collected at the same time is 0.4 ppb. This pair difference value includes flasks measured at some sites that were not included in the subset of sites used in this study, and so may not be entirely representative for this study. A single aliquot of air from each flask is analyzed for N_2O, and the measurements from each member are averaged to give the N_2O mole fraction for that sample. In addition to N_2O, samples are also analyzed for CH_4, CO_2, CO, H_2, SF_6, and $\delta^{13}C$ and $\delta^{18}O$ in CO_2.

[12] Measurements of N_2O began in June 1997 for most of the Cooperative Global Air Sampling Network. While measurements are ongoing, we ended our study at the end of 2001 since we lacked the NCEP-based transport fields to run the 3.75° latitude × 5° longitude TM3 model after that time. The locations of the 48 surface sites used in this study are shown in Figure 3. We have excluded several sites that either have large gaps in the data (e.g., Summit, Greenland) or that are strongly influenced by nearby N_2O sources that cannot be resolved with the coarse resolution of the model (e.g., Tae-Ahn Peninsula, Korea; Hungary and Baltic sites). We do not include sites that started sampling after December 2001 or that were discontinued before 1997, since they do not provide any data during our study period. Mountain sites (e.g., Kazakhstan; Izãna, Canary Islands) are also not included because these sites are likely to be more influenced by downwelling stratospheric air which is a large source of uncertainty in this study. For each station, we calculate the

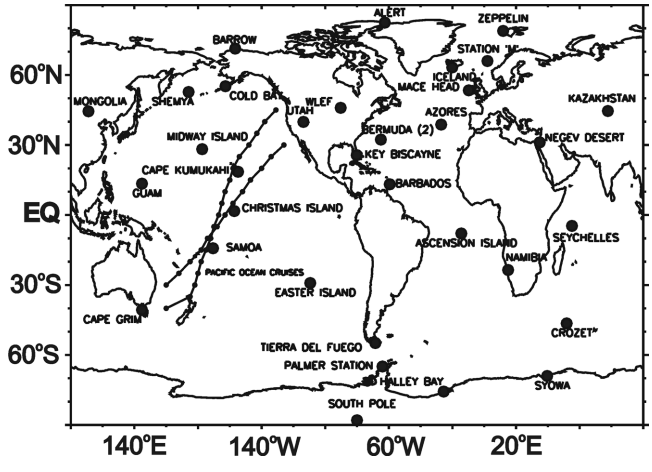

Figure 3. Map of the 48 sites in the NOAA/ESRL GMD CCGG Cooperative Global Air Sampling Network used in this analysis. Information on each site can be found at the NOAA/ESRL GMD CCGG Interactive Atmospheric Data Visualization web site: http://www.cmdl.noaa.gov/ccgg/iadv, or see *Dlugokencky et al.* [1994]. Two Pacific ship tracks are shown by the connected points in the Pacific Ocean.

monthly mean of the flask measurements for all months with at least three flask samples in the month (see Table 1). For the 48 stations used in this study, there were 1695 station-months available that met this criterion from June, 1997 to December, 2001. Comparison with independent measurements from the Advanced Global Atmospheric Gases Experiment (AGAGE) program (the data are available through the Carbon Dioxide Information Analysis Center (CDIAC) at http://cdiac.ornl.gov/ftp/ale_gage_Agage/AGAGE and discussed by *Prinn et al.* [2000]) show that the latitudinal gradient measured by the two programs only differ by a couple of tenths of a ppb at most (Figure 4). Therefore we can be confident that the inverse modeling technique will be interpreting a robust spatial pattern. The average concentrations from June 1997 through December 2001 are shown for Cape Grim (Australia), American Samoa, Ragged Point (Barbados), and Mace Head (Ireland), with the Cape Grim concentration subtracted from each site.

[13] For use in the inverse modeling, 312.0 ppb was subtracted from the time series at all sites before the inversion (so that the fluxes would only have to account for the latitudinal gradient and changes in the atmospheric burden after 1997 and not the entire atmospheric burden) and a trend was added to all sites to simulate the stratospheric loss term in the budget (see section 2.7). The inverse technique required an initial adjustment period to match the latitudinal gradient, so we discarded the first year of inferred fluxes and only analyzed the 1998–2001 results. We chose this approach for simplicity, because any initial latitudinal gradient (for example generated with a priori fluxes) will have limited accuracy, and still require an initial adjustment period.

2.3. Transport Model 3 (TM3)

[14] To generate the Green's functions (also known as response functions) for the inversion, we used TM3 version 3.2 [*Heimann*, 1995; *Heimann and Körner*, 2003], with a horizontal resolution of 3.75° latitude by 5° longitude, and with 19 vertical levels. The Green's functions were created in TM3 by simulating the release of N_2O from each region (treating the N_2O from each region as a different species) into the atmosphere at the rate of 1 MtN_2O yr^{-1} for 1 month and storing the resulting monthly averaged three-dimensional N_2O concentration field for 12 months. As discussed below, we consider two spatial distributions of this "unit" flux to assess the sensitivity of the inversion to the flux pattern assumed for each region: (1) patterning of the flux within regions identical to the scaling in the GEIA inventory and (2) even distribution of the flux across the region. The three-dimensional concentration field was then sampled to build a matrix containing the sensitivity of each measurement site to the flux from each of the regions. This procedure was done for each month from January 1997 to December 2001. Because the inversion was done offline, it was necessary to extrapolate the response functions to account for the effect of atmospheric mixing that occurred farther out than 12 months. This extrapolation was done assuming exponential decay of the response function with a time constant of 100 days to an asymptote value of 0.011 ppb. These parameters were determined by fitting an exponential curve to the tail of the response functions. The asymptote was the same as the value calculated using a conversion factor of 1 ppb = 4.8 MtN [*Kroeze et al.*, 1999]. The asymptote value was slightly different depending on the number of days in the month. While the inversion was done in units of MtN_2O, the results are all presented in MtN.

2.4. A Priori Fluxes

[15] We used the IGBP/IGAC GEIA inventory [*Bouwman et al.*, 1995], which is available to the public (http://www.geiacenter.org/presentData/n2o.html). The data set includes the annual total of natural and anthropogenic nitrous oxide sources on a 1° × 1° grid. There is no information about seasonal variability included in the inventory. The GEIA inventory includes nine source types: (1) natural and fertilized soils, (2) animal waste, (3) enhanced fluxes from cleared land, (4) oceanic, (5) industrial, (6) fossil fuel burning, (7) biofuel burning, (8) agricultural waste burning, and (9) biomass burning. The inventory represents the annual total for the year 1990, as described by *Bouwman et al.* [1995]. The global total inventory source equals 13.5 MtN yr^{-1}, which is somewhat lower than the *Prather and Ehhalt* [2001] estimate of 16.4 MtN yr^{-1} or our estimate in section 1 of ~16 MtN yr^{-1}. While the GEIA inventory is a bottom up inventory, constructed using process models and flux measurements, the "best case" scenario from *Bouwman et al.* [1995] chosen for the GEIA inventory was the one most consistent with the results of *Prinn et al.* [1990]. The discrepancy in the global total most likely relates to the stratospheric loss assumed in the two cases, since the atmospheric increase is well known from measurements. A global source of 13.5 MtN yr^{-1} balances the atmospheric increase plus a stratospheric loss resulting from a lifetime of 166 years. Since the GEIA inventory [*Bouwman et al.*, 1995] was designed to be consistent with the study of *Prinn et al.* [1990], which used a lifetime of 166 (±16) years based on the then-available model calculations, this global total makes sense. A source of 16.4 MtN yr^{-1} is more consistent with the currently accepted lifetime of ~120 years [*Prinn et al.*, 1998; *Prather and Ehhalt*, 2001]. The inverse calculation allowed us to analyze where the additional ~3 MtN yr^{-1} was allocated to be consistent with the atmospheric observations, given the relative uncertainties of the prior flux from different regions. A map of the total GEIA N_2O source on a 1° × 1° grid is shown in Figure 5. On land, tropical and industrialized Northern Hemisphere temperate regions stand out as large sources. In the ocean, the eastern tropical Pacific, the Southern Ocean, and the northern Pacific also stand out (see *Nevison et al.* [1995] for a discussion of these features).

2.5. Bayesian Inversion

[16] As discussed by *Enting* [2002], the inverse problem in a Bayesian framework is to determine the probability density of surface fluxes conditional on our measured atmospheric concentrations and a priori information about fluxes and their uncertainties, given a modeled relationship between fluxes and measurements. Formally, the Bayesian

Table 1. NOAA/ESRL GMD CCGG Cooperative Global Air Sampling Network Sites Used in This Study

Site Code	Name	Latitude	Longitude	Altitude, m.a.s.l.	Cooperating Agency	Months With N ≥ 3
ALT	Alert, Nunavut, Canada	82.45	−62.52	210	Environment Canada/ Meteorological Service of Canada	50
ASC	Ascension Island, United Kingdom	−7.92	−14.42	54	USAF/Computer Science Raytheon	45
AZR	Terceira Island, Azores, Portugal	38.77	−27.38	40	Instituto Nacional de Meteorologia e Geofisica	40
BME	St. David's Head, Bermuda, United Kingdom	32.37	−64.65	30	Bermuda Biological Station	50
BMW	Tudor Hill, Bermuda, United Kingdom	32.27	−64.88	30	Bermuda Biological Station	44
BRW	Barrow, Alaska, United States	71.32	−156.60	11	NOAA CMDL	49
CBA	Cold Bay, Alaska, United States	55.20	−162.72	25	U.S. National Weather Service	49
CGO	Cape Grim, Tasmania, Australia	−40.68	144.68	94	CSIRO, Atmospheric Research	49
CHR	Christmas Island, Republic of Kiribati	1.70	−157.17	3	Dive Kiribati	26
CRZ	Crozet Island, France	−46.45	51.85	120	Centre des Faibles Radioactivities/TAAF	39
EIC	Easter Island, Chile	−27.15	−109.45	50	Direccion Meteorologica de Chile	48
GMI	Mariana Islands, Guam	13.43	144.78	6	University of Guam/ Marine Laboratory	50
HBA	Halley Station, Antarctica, United Kingdom	−75.58	−26.50	33	British Antarctic Survey	54
ICE	Storhofdi, Vestmannaeyjar, Iceland	63.34	−20.29	127	Icelandic Meteorological Service	43
KEY	Key Biscayne, Florida, USA	25.67	−80.20	3	NOAA AOML	45
KUM	Cape Kumukahi, Hawaii, USA	19.52	−154.82	3	NOAA CMDL	49
KZD	Sary Taukum, Kazakhstan	44.45	75.57	412	Kazakh Scientific Institute of Environmental Monitoring and Climate	46
LEF	Park Falls, Wisconsin, United States	45.93	−90.27	868	Wisconsin Educational Communications Board	48
MHD	Mace Head, County Galway, Ireland	53.33	−9.90	25	University College Galway	49
MID	Sand Island, Midway, United States	28.21	−177.38	7.7	U.S. Fish and Wildlife Service	48
NMB	Gobabeb, Namibia	−23.58	15.03	461	Desert Research Foundation of Namibia	21
POC	Pacific Ocean, N/A	Variable	Variable	10	Volunteer Observing Ship Program	Varies
PSA	Palmer Station, Antarctica, United States	−64.92	−64.00	10	National Science Foundation	48
RPB	Ragged Point, Barbados	13.17	−59.43	45	Private Party	48
SEY	Mahe Island, Seychelles	−4.67	55.17	7	Seychelles Bureau of Standards	49
SHM	Shemya Island, Alaska, United States	52.72	174.10	40	PIQUNIQ Management Corporation	48
SMO	Tutuila, American Samoa	−14.24	−170.57	42	NOAA CMDL	50
SPO	South Pole, Antarctica, United States	−89.98	−24.80	2810	NOAA CMDL and National Science Foundation	43
STM	Ocean Station M, Norway	66.00	2.00	5	Norway Meteorological Institute	49
SYO	Syowa Station, Antarctica, Japan	−69.00	39.58	14	National Institute of Polar Research	46
TDF	Tierra Del Fuego, La Redonda Isla, Argentina	−54.87	−68.48	20	Servicio Meteorologico Nacional	21
UTA	Wendover, Utah, United States	39.90	−113.72	1320	U.S. National Weather Service	48
UUM	Ulaan Uul, Mongolia	44.45	111.10	914	Mongolian Hydrometeorological Research Institute	47
WIS	Sede Boker, Negev Desert, Israel	31.13	34.88	400	Weizmann Institute of Science	48
ZEP	Ny-Alesund, Svalbard, Norway and Sweden	78.90	11.88	475	Institute of Applied environmental Research, Stockholm University	47

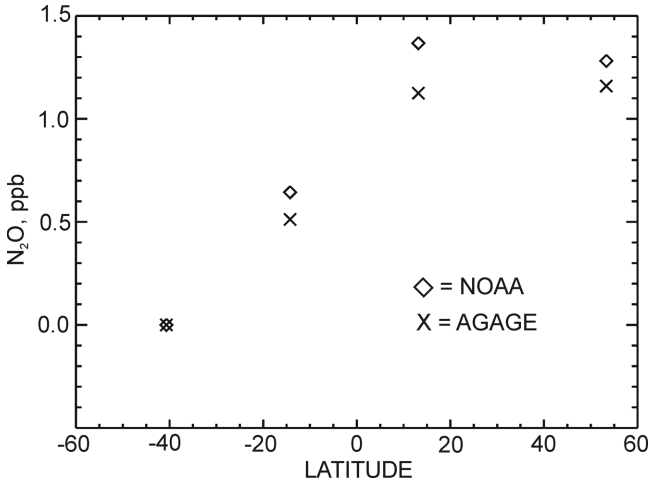

Figure 4. Comparison of the 1998–2001 average latitudinal gradient based on data used in this study and on data from the AGAGE program.

relationship between the unknown fluxes (s) we are estimating and measurements (z) is

$$p(s|z) = \frac{p(z|s)p(s)}{\int p(z|s)p(s)ds}. \quad (1)$$

In our application, $p(s|z)$ is the probability distribution of the inferred, or a posteriori fluxes given the available data. The term $p(z|s)$ is the probability distribution of the available data for a given set of fluxes and p(s) is the prior probability distribution of the unknown fluxes. We are trying to maximize $p(s|z)$, which is equivalent to minimizing the following objective function J:

$$J = \frac{1}{2}(\mathbf{z} - \mathbf{Hs_p})^T \mathbf{R^{-1}}(\mathbf{z} - \mathbf{Hs_p}) + \frac{1}{2}(\mathbf{s} - \mathbf{s_p})^T \mathbf{Q}^{-1}(\mathbf{s} - \mathbf{s_p}). \quad (2)$$

Here $\mathbf{z}$ represents our measurement vector, $\mathbf{s_p}$ the vector of prior fluxes, and $\mathbf{s}$ the vector of a posteriori fluxes. $\mathbf{R}$ and $\mathbf{Q}$ are the covariance matrices of the model-data mismatch and prior error, respectively. Model-data mismatch error is a combination of measurement precision, the ability of the transport model to reproduce measurements given perfect surface fluxes, and any errors in specifying flux patterns within aggregated regions (so-called aggregation error). $\mathbf{H}$ is the matrix of Green's functions (also called response functions), which represent the modeled relationship between emissions in each region at a given time to the concentrations measured at each measurement location over time (see section 2.3). The most probable set of posterior fluxes $\hat{\mathbf{s}}$, found by taking the derivative of equation (2) with respect to $\mathbf{s}$ and setting it equal to zero, is

$$\hat{\mathbf{s}} = \mathbf{s_p} + \mathbf{QH}^T(\mathbf{HQH}^T + \mathbf{R})^{-1}(\mathbf{z} - \mathbf{Hs_p}). \quad (3)$$

In our setup, both $\mathbf{R}$ and $\mathbf{Q}$ are diagonal matrices, reflecting our assumption that model-data mismatch errors are independent between measurement sites and prior errors are independent between regions. The transport matrix $\mathbf{H}$ has dimensions (M × N) because it relates the M concentration measurements to N fluxes. The Bayesian least squares approach also yields an estimate of the posterior covariance,

$$\hat{\mathbf{Q}} = \mathbf{Q} - \mathbf{QH}^T(\mathbf{HQH^T} + \mathbf{R})^{-1}\mathbf{HQ}. \quad (4)$$

Equation (4) is derived by taking the inverse of the Hessian (second derivative) of equation (2) with respect to $\mathbf{s}$.

2.6. Determining Model-Data Mismatch and Prior Flux Uncertainty

[17] Model-data mismatch and prior flux uncertainties were calculated using a Maximum Likelihood method [*Michalak et al.*, 2005]. The most likely values of the uncertainties in the $\mathbf{Q}$ and $\mathbf{R}$ matrices were calculated by minimizing the negative logarithm of the probability density function of the uncertainties, given a set of measurements, prior fluxes, and atmospheric transport (which are treated as fixed in the optimization),

$$L_\theta = \frac{1}{2}\ln|\mathbf{HQH}^T + \mathbf{R}| + \frac{1}{2}(\mathbf{z} - \mathbf{Hs_p})^T(\mathbf{HQH}^T + \mathbf{R})^{-1}(\mathbf{z} - \mathbf{Hs_p}). \quad (5)$$

[18] In equation (5), the | | symbol denotes a matrix determinant. The minimization was done using a Gauss-Newton method as described by *Michalak et al.* [2005]. The method guarantees that the reduced chi-square value for both fluxes and measurements is equal to 1, although this is not the criterion used in estimating the covariance parameters. In other words, the differences between the a priori and a posteriori fluxes are consistent with the a priori flux uncertainty found using this method; at the same time, the

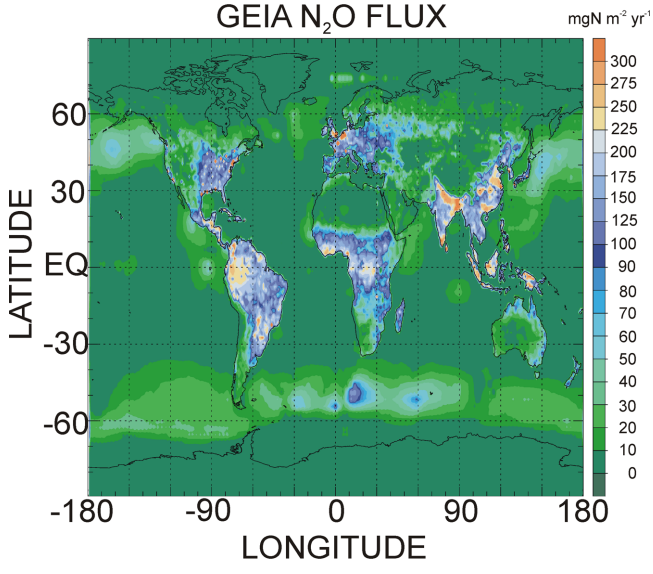

Figure 5. Map of total annual flux included in the GEIA inventory.

Table 2a. A Priori Flux Uncertainty and Model-Data Mismatch Error for Four Semihemisphere Basis Regions[d]

	A Priori Flux Uncertainty 90°S–30°S,[a] MtN yr^{-1}	A Priori Flux Uncertainty 30°S to Equator,[b] MtN yr^{-1}	A Priori Flux Uncertainty Equator to 30°N,[c] MtN yr^{-1}	A Priori Flux Uncertainty 30°N–90°N,[d] MtN yr^{-1}	Model-Data Mismatch Error: Land and Ship Sites, ppb	Model-Data Mismatch Error: Other Sites, ppb
Fluxes distributed like GEIA	2.1	3.6	6.6	2.0	0.3	0.2
Fluxes evenly distributed	2.0	2.4	6.6	2.1	0.3	0.2

[a]A priori flux = 2.0 MtN yr^{-1}.
[b]A priori flux = 3.4 MtN yr^{-1}.
[c]A priori flux = 4.0 MtN yr^{-1}.
[d]A priori flux = 4.1 MtN yr^{-1}.

differences between observed N_2O and N_2O predicted by transporting the a posteriori fluxes forward in TM3 are consistent with the model-data mismatch values found using this method. This method assumes no prior knowledge of the uncertainty parameters. In addition, flux regions and measurement sites can be grouped together (in the sense that they are assumed to have the same error) in different arrangements when solving for the uncertainty parameters. For example, if it is thought that the transport model has more difficulty matching measurements taken over the continents than over oceans, land and ocean measurement sites can be grouped and separate model-data mismatch variances calculated for each group. If there is no difference in the model-data mismatch for different groupings, the method will show that this is the case. In this study, the prior uncertainty was determined separately for each semihemispherical basis region (Table 2a, shown as 1σ uncertainty). For the 22 TransCom3 regions, tropical regions and the Southern Ocean were grouped separately from the other regions (Table 2b). Basis regions were grouped in this way because we noted that tropical regions and the Southern Ocean tended to depart more from the a priori estimates than other regions, and concluded that their prior estimates were probably more uncertain. Measurement sites were divided into two groups: continental and shipboard measurements were considered separately from the other sites, which are mainly remote marine boundary layer sites. Continental and shipboard measurements showed higher variability, so we hypothesized they might be harder to model, similar to assumptions made in previous studies for model-data mismatch. Note that the model-data mismatch values in Tables 2a and 2b are shown as 1σ (the square root of the variance) and do not include the uncertainty in the influence of the stratospheric loss on the surface measurements, which are added separately. The model-data mismatch values are comparable with the precision of the N_2O measurements, perhaps due in part to the averaging of multiple weeks of data to yield monthly average values, effectively smoothing the data. Slightly different values were found for the flux uncertainty and model-data mismatch when fluxes were assumed to be distributed evenly across basis regions as opposed to being given the same relative distribution as the GEIA fluxes.

2.7. Influence of Stratosphere-Troposphere Exchange (STE) on Surface Measurements

[19] The influence of downwelling N_2O-poor stratospheric air (which is depleted by photochemical loss above 50 hPa and returns to the troposphere in the extratropics via large-scale atmospheric circulation) on surface measurements is a large source of uncertainty in this study. However, it is important to explicitly model this influence, since the dilution of tropospheric N_2O resulting from stratosphere-troposphere exchange (STE) almost balances the enrichment caused by the surface sources. Thus this term in the N_2O budget likely affects the temporal and spatial variability of surface N_2O to a similar degree as the fluxes [*Levy et al.*, 1982; *Prinn et al.*, 1990]. Two different approaches are used in this study to quantify the influence of the stratospheric sink on the surface measurements and to explore the sensitivity of the inverse modeling results to the treatment of the stratospheric sink. The first approach is to specify stratospheric N_2O in the top three levels of TM3, using data from the Cryogenic Limb Array Etalon Spectrometer (CLAES) instrument on the Upper Atmospheric Research Satellite (UARS) [*Kumer et al.*, 1993; *Randel et al.*, 1994; *Gettelman et al.*, 1997]. These data, provided by William Randel (NCAR), are available via the WCRP SPARC (Stratospheric Processes and their Role in Climate) Data Center (http://sparc.sunysb.edu/html/uars_index.html).

Table 2b. A Priori Flux Uncertainty and Model-Data Mismatch Error for 22 Transcom3 Basis Regions

	A Priori Flux Uncertainty: Tropical and Southern Ocean, MtN yr^{-1}	A Priori Flux Uncertainty: Other Regions, MtN yr^{-1}	Model-Data Mismatch Error: Land and Ship Measurement Sites, ppb	Model-Data Mismatch Error: Other Sites, ppb
Fluxes distributed like GEIA	1.6	0.6	0.3	0.2
Fluxes evenly distributed	1.5	0.4	0.3	0.2

The data set includes the N_2O seasonal cycle (12 monthly means) for 16 pressure levels ranging from 100 hPa to 0.32 hPa, and covers 80S to 80N in 4 degree increments. To implement the CLAES measurements in TM3, we interpolated them linearly in space and time and used them to prescribe the mixing ratio for the top three levels (centered at 10, 30, and 50 mb) of TM3. Latitudes poleward of 80 degrees were given the same mixing ratio as that found at 80 degrees. The mixing ratio below 50 hPa was initialized with a uniform 320 ppb. There was no source of N_2O at the surface, so that we only saw the influence of the stratospheric destruction and atmospheric mixing. Then we ran the TM3 model forward with prescribed CLAES concentrations and no surface source from 1995–2001 using the NCEP analyzed wind fields. There was a period of 2 years during which the initial modeled vertical profile adjusted to the large-scale atmospheric transport. After about 5 years the model approached a profile that balanced the stratospheric loss (implicit in our fixed stratospheric mixing ratios) with vertical transport. This vertical profile decreased very slowly in the extratropics as the atmospheric mixing ratios below 50 hPa decreased. We extracted the daily mean surface mixing ratio from the final year (2001) of the simulation at each of our 48 sites. The monthly mean mixing ratio at each site and their standard deviations (i.e., of the daily values going into the monthly mean) were calculated. The latitudinal gradient in each month was detrended by subtracting the mean of the mixing ratio across the 48 sites for that month. This detrending was necessary since we did not simulate any surface fluxes to balance the stratospheric destruction, so that the atmospheric concentration slowly decreased. The variances of the monthly average mixing ratios were added to the values in the matrix R (model-data mismatch) for the inverse calculation. The monthly latitudinal gradients resulting from the stratospheric destruction were then presubtracted from the measurements to simulate the influence of downwelling stratospheric air on the measured latitudinal gradient. We also added a trend of 2.65 ppb yr^{-1} to the measurements to simulate the globally averaged impact of the stratospheric loss on the surface measurements. To incorporate the uncertainty in the lifetime of N_2O we considered scenarios where we added 3.3 ppb yr^{-1} or 2.2 ppb yr^{-1} to the measurements, corresponding to a lifetimes of 98 (best estimate of the lifetime minus 1σ) and 146 (best estimate plus 1σ) years [*Volk et al.*, 1997]. The zonally and annually averaged surface mixing ratio resulting from the CLAES-based stratospheric mixing ratio constraint shows more influence in the Southern Hemisphere by several tenths of a ppb (Figure 6a). This result is likely due to the very low concentrations in the SH polar vortex during the Antarctic winter [see *Randel et al.*, 1994], combined with the pattern of mass fluxes in TM3 used in this study.

[20] The second approach was to use response (Green's) functions to model the sensitivity of the surface mixing ratio to the downwelling stratospheric air. Each year, the general circulation of the atmosphere transfers a net flux of approximately −12.3 MtN yr^{-1} through the tropopause into the extratropical troposphere (assuming a lifetime of 122 years), which is manifested as a dilution of tropospheric N_2O by an influx of N_2O-poor stratospheric air. In simple terms, the general circulation is mixing the photochemical loss that occurs above 50 hPa down into the troposphere. Since there is no further photochemistry below 50 hPa, we can apply this loss rate at the top of the troposphere. We chose this approach rather than explicitly modeling the stratospheric photochemical sink because of concern that the coarsely resolved stratosphere in this version of TM3 would be unable to accurately represent both the photochemistry and stratosphere-troposphere exchange. Since we have more

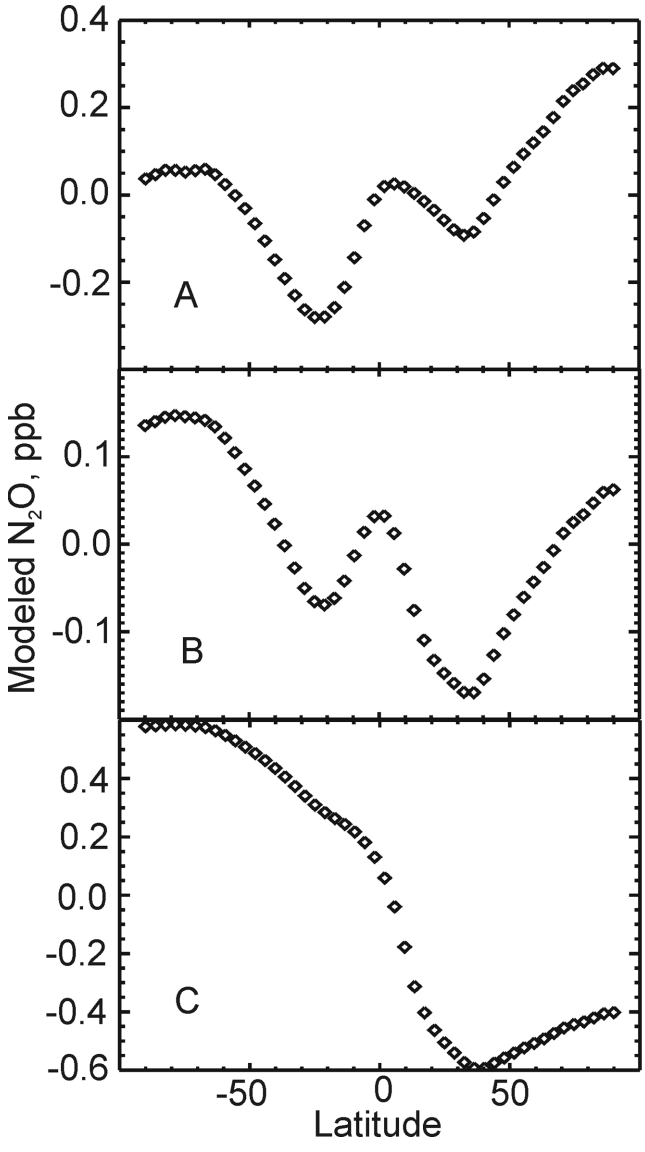

Figure 6. Annual average latitudinal gradient resulting from the different treatments of the stratospheric flux: (a) using CLAES data to specify the top three levels in TM3; (b) using response functions to calculate the response to the stratospheric loss, dividing the loss evenly between the two hemispheres; and (c) using response functions, but splitting the annual loss such that two thirds is applied to the NH and one third to the SH.

Table 3. Scenarios Considered in This Study

Case	N_2O Lifetime, years	STE Assumptions[a]	Distribution of Fluxes Within Regions	Additional Changes
A	122	RF, loss evenly distributed	distributed like GEIA	N/A
B	122	RF, loss unevenly distributed	distributed like GEIA	N/A
C	122	RF, loss evenly distributed	distributed like GEIA	a priori flux scaled by 1.36
D	122	RF, loss unevenly distributed	distributed like GEIA	a priori flux scaled by 1.36
E	122	RF, loss evenly distributed	Evenly distributed	N/A
F	122	RF, loss unevenly distributed	evenly distributed	N/A
G	122	CLAES	distributed like GEIA	N/A
H	98	RF, loss evenly distributed	distributed like GEIA	N/A
I	98	RF, loss unevenly distributed	distributed like GEIA	N/A
J	146	RF, loss evenly distributed	distributed like GEIA	N/A
K	146	RF, loss unevenly distributed	distributed like GEIA	N/A

[a]RF, response functions used; CLAES, CLAES data used to constrain stratospheric concentrations. Loss evenly distributed denotes half of annual stratospheric loss applied to NH and half to SH. Loss unevenly distributed denotes two thirds applied to NH and one third to SH.

confidence in the modeled tropospheric transport, we sought to introduce a signal at the troposphere representing stratosphere-troposphere exchange which could then be mixed down to the surface. In the same way that our surface response functions represent the response of atmospheric N_2O to a flux at the surface, we also use basis functions in the upper troposphere/lower stratosphere to model the response of the troposphere to this negative flux, analogous to how *Randerson et al.* [2002] used response functions to model the input of radiocarbon from the stratosphere into the troposphere. We defined basis regions from 30°S–90°S and 30°N–90°N at 194 hPa (level 13 in TM3), and emitted N_2O from these regions at the rate of 1 MtN yr^{-1} for 1 month at a time, from January 1997 through December 2001. While we treated STE as evenly distributed between 30°N and 90°N there may be a different spatial pattern in reality. However, this approach did give promising results in the case of bomb radiocarbon [*Randerson et al.*, 2002]. The daily mean mixing ratio response at the surface was saved for 36 months at each of the 48 sites. This daily mean mixing ratio response (ppb (MtN $yr^{-1})^{-1}$) was multiplied by the annual loss rate of N_2O to produce the ppb response at the surface. We used −12.3, −15.3, or −10.3 MtN yr^{-1} to represent the stratospheric loss, corresponding to a lifetime of 122, 98, or 146 years to include the uncertainty in the lifetime. This total flux was either divided evenly between the two hemispheres (as suggested by *Appenzeller et al.* [1996] and *Schoberl* [2004]), or weighted more toward the Northern Hemisphere, to reflect stronger downwelling in that hemisphere [*Gettelman and Sobel*, 2000]. We chose a two-thirds weighting in the NH and one-third weighting in the SH as an end-member to assess the sensitivity of the inverse modeling results to this weighting. We also applied a seasonality to the flux in each hemisphere, using the same seasonality as *Randerson et al.* [2002] (corresponding to Figure 8 of *Appenzeller et al.* [1996]) which gave reasonable results for the seasonal cycle of radiocarbon at the surface in their study. Once the monthly mean flux was multiplied by the response functions to give mixing ratio responses, the influence of the two upper troposphere/lower stratosphere basis regions for all months were added together to get the mixing ratio response at the surface. We then calculated the seasonal cycle of the monthly mean latitudinal gradients. These were presubtracted from the measurements and the variance of the daily means used to calculate the monthly mean values were added to the R matrix for the inverse modeling. These added variances were generally very small, with standard deviations less than 0.2 ppb. The zonally and annually averaged latitudinal gradient caused by an annual loss of 12.3 MtN yr^{-1} evenly divided between the two hemispheres is very different from the case where two thirds is added to the Northern Hemisphere and one third to the Southern Hemisphere (Figures 6b and 6c). Both are different from the CLAES-constrained case, such that we feel that the combination of the three cases provides a good test of the sensitivity of the inverse model results to treatment of the stratospheric sink.

2.8. Cases Considered in This Study

[21] We considered 11 different cases to assess the sensitivity of the inverse modeling results to different sources of uncertainty (see Table 3). Our ''base case'' (case A) corresponds to the following assumptions: (1) 122-year lifetime of N_2O; (2) fluxes within regions distributed with the same scaling as the GEIA inventory; and (3) upper troposphere/lower stratosphere response functions used to model the influence of downwelling stratospheric air, with the total dilution evenly split between the two hemispheres. We vary each of these assumptions as follows: (1) We use lifetimes of 98 and 146 years to address the uncertainty in the global N_2O lifetime and for each we test the sensitivity to how the STE flux signal is divided between hemispheres (evenly versus two thirds in the Northern Hemisphere and one third in the Southern Hemisphere); (2) using a lifetime of 122 years, we assume evenly distributed fluxes within basis regions and test the sensitivity to how the STE signal is divided; (3) using a lifetime of 122 years, we use the CLAES data in TM3 to assess the influence of downwelling stratospheric air; and (4) we assume a lifetime of 122 years, use the GEIA inventory to distribute the flux within basis regions, and test the sensitivity to how the STE signal is divided, but scale our prior flux by 1.36 (166/122) to make it more consistent with the *Volk et al.* [1997] lifetime.

3. Results

3.1. Global Total Flux

[22] The inferred global total flux (Tables 4a and 4b) for both sets of basis regions (semihemispheres versus Trans-

Table 4a. The 1998–2001 Flux (1σ) for Semihemispheres[a]

	GEIA	A	B	C	D	E	F	G	H	I	J	K
90°S–30°S	2.0 (2.1)	0.2 (0.5)	−0.2 (0.5)	0.2 (0.6)	−0.2 (0.6)	0.8 (0.5)	0.1 (0.6)	0.3 (0.5)	0.6 (0.5)	0.1 (0.5)	0.0 (0.5)	−0.4 (0.5)
30°S to equator	3.4 (3.6)	4.7 (1.6)	2.9 (1.6)	4.9 (1.1)	3.0 (1.1)	4.3 (1.6)	3.1 (1.1)	5.6 (1.6)	5.7 (1.6)	3.4 (1.6)	4.1 (1.5)	2.5 (1.5)
Equator to 30°N	4.1 (6.6)	9.3 (1.6)	10.8 (1.7)	9.1 (1.4)	10.6 (1.4)	9.3 (1.7)	10.5 (1.4)	8.7 (1.6)	10.4 (1.7)	12.4 (1.7)	8.5 (1.6)	9.8 (1.6)
30°N–90°N	4.0 (2.0)	3.1 (0.6)	3.8 (0.6)	3.2 (0.6)	3.9 (0.6)	2.8 (0.6)	3.5 (0.6)	2.7 (0.6)	3.6 (0.6)	4.6 (0.6)	2.7 (0.6)	3.3 (0.6)
Total Globe	13.5 (8.1)	17.3 (1.4)	17.3 (1.4)	17.4 (1.4)	17.4 (1.4)	17.2 (1.4)	17.2 (1.4)	17.3 (1.4)	20.4 (1.5)	20.4 (1.5)	15.2 (1.4)	15.2 (1.4)

[a]Unit is MtN yr^{-1}.

Com3 super regions) was 17.2–17.4 MtN yr^{-1} with a posteriori uncertainty of about 1.4 MtN yr^{-1} (1σ), when assuming a 122-year lifetime. The uncertainty of the global total was calculated by summing all the elements in the a posteriori covariance matrix (including both diagonal and off-diagonal elements) corresponding to the monthly fluxes from 1998–2001, dividing by the number of months (48), and taking the square root of the resulting average variance. Taking into account the uncertainty in the lifetime of N_2O (cases H–K) this range expands to 15.2–20.4 MtN yr^{-1}. This a posteriori flux was much higher than the prior flux of 13.5 ± 5.4 MtN yr^{-1} except for cases C and D, where the prior flux was scaled by 1.36 (166/122) to make it more consistent with a 122-year lifetime. As mentioned earlier, the a posteriori flux was higher because we assumed a larger stratospheric loss term in the global budget relative to the prior case. When the prior flux was scaled by 1.36 (cases C and D), the global totals for a priori and a posteriori were obviously the same. The uncertainty of the a posteriori global flux was only about 26% of the a priori uncertainty (1σ) because the globe as a whole is well sampled by the air sampling network.

[23] We aggregated the semihemispherical basis regions into Northern and Southern Hemisphere totals, in order to calculate their ratio. The results depend very strongly on the treatment of the stratospheric loss. Not surprisingly, the lowest ratio of 1.9 is found when using the CLAES-constrained treatment of the stratospheric loss, since that treatment actually predicts a greater lowering of the measurements in the Southern Hemisphere by STE (which is subtracted from the data before the inversion). When using response functions to model the influence of the stratospheric loss on the surface measurements, the ratio ranges from about 2 to 2.5 when the total stratosphere-troposphere extratropical flux is divided evenly between hemispheres. The ratio is closer to 4–5 when two thirds of the stratosphere-troposphere flux is applied to the NH and one third to the SH, since this treatment has a strong impact on the latitudinal gradient used in the inverse calculation. All the results are somewhat higher than earlier estimates of about 1.5 to 2.0 [*Butler et al.*, 1989; *Cicerone*, 1989; *Prinn et al.*, 1990], suggesting that the cases resulting in ratios of 4–5 may be unrealistic.

[24] The TransCom3 super regions were also further aggregated to divide the global flux into terrestrial and ocean contributions. For the cases with a 122-year lifetime, the global total terrestrial flux ranged from 10.7 (case G) to 12.7 (case F) MtN yr^{-1} and the total ocean flux ranged from 4.5 (case F) to 6.5 (case G) MtN yr^{-1}, such that the oceans represented about 26–36% of the global total flux, using the central values of the inferred fluxes. The inferred ocean total is consistent with the *Nevison et al.* [1995] study (1.2–6.8 MtN yr^{-1}) which used air-sea Δp_{n2o} measurements and modeled daily air-sea gas exchange coefficients to calculate the global ocean flux. It is also consistent with the results of a more recent study based on subsurface N_2O measurements that calculated a global ocean source of 5.8 ± 2 MtN yr^{-1} [*Nevison et al.*, 2003]. The oceanic contribution to the global total is also near the a priori value of 29%. If the preindustrial source of N_2O was 10.4–11 MtN yr^{-1} (see section 1) and we assume that the oceanic flux has not changed, we estimate the preindustrial terrestrial source to have been about 3.9–6.5 MtN yr^{-1}. The high end of this preindustrial terrestrial flux estimate is consistent with process model-derived estimates of the N_2O flux from natural soils [*Bouwman et al.*, 1993; *Potter et al.*, 1996; *Nevison et al.*, 1996]. The difference between our inferred total terrestrial flux and the estimate of the preindustrial terrestrial flux yields an anthropogenic terrestrial flux enhancement of between 4 and 9 MtN yr^{-1}. This estimate is similar to the results of *Kroeze et al.* [1999] which found the total anthropogenic contribution to be 8.0 MtN yr^{-1} in 1994, dominated by agricultural emissions (6.2 MtN yr^{-1}). *Prather and Ehhalt* [2001] place the anthropogenic contribution at 5.7 MtN yr^{-1}. It is somewhat easier to fit this lower estimate of the anthropogenic origin plus estimates of

Table 4b. The 1998–2001 Flux (1σ) for TRANSCOM3 Super Regions[a]

	GEIA	A	B	C	D	E	F	G	H	I	J	K
North Land	3.6 (1.4)	2.7 (0.7)	3.3 (0.7)	2.9 (0.7)	3.5 (0.7)	2.6 (0.5)	3.1 (0.5)	2.3 (0.7)	3.1 (0.7)	3.8 (0.7)	2.5 (0.7)	3.0 (0.7)
Tropical Land	3.8 (2.9)	5.9 (2.2)	6.7 (2.2)	5.7 (2.2)	6.6 (2.2)	6.8 (1.8)	8.0 (1.8)	5.8 (2.1)	6.9 (2.2)	7.9 (2.2)	5.2 (2.1)	5.9 (2.1)
South Land	2.0 (1.9)	2.3 (1.3)	1.6 (1.3)	2.6 (1.3)	1.8 (1.3)	2.4 (1.0)	1.6 (1.0)	2.6 (1.3)	2.8 (1.3)	1.8 (1.3)	2.1 (1.3)	1.4 (1.3)
North Ocean	1.2 (1.0)	1.7 (0.7)	2.0 (0.7)	1.8 (0.7)	2.1 (0.7)	1.7 (0.5)	1.9 (0.5)	1.7 (0.7)	1.8 (0.7)	2.2 (0.7)	1.6 (0.7)	1.8 (0.7)
Tropical Ocean	0.9 (3.3)	4.1 (2.0)	3.8 (2.0)	3.6 (2.0)	3.4 (2.0)	3.1 (1.5)	2.6 (1.5)	4.0 (2.0)	4.7 (2.0)	4.5 (2.0)	3.6 (2.0)	3.4 (2.0)
South Ocean	1.7 (2.0)	0.6 (0.7)	−0.1 (0.7)	0.6 (0.7)	−0.1 (0.7)	0.7 (0.5)	0.0 (0.5)	0.8 (0.7)	1.0 (0.7)	0.1 (0.7)	0.3 (0.7)	−0.3 (0.7)
Total Land	9.4 (3.7)	10.9 (1.4)	11.6 (1.4)	11.3 (1.4)	12.0 (1.4)	11.8 (1.3)	12.7 (1.3)	10.7 (1.4)	12.8 (1.4)	13.6 (1.4)	9.7 (1.4)	10.3 (1.4)
Total Ocean	3.8 (3.8)	6.3 (1.2)	5.7 (1.2)	6.1 (1.2)	5.4 (1.2)	5.4 (1.1)	4.5 (1.1)	6.5 (1.2)	7.6 (1.3)	6.8 (1.3)	5.5 (1.2)	4.9 (1.2)
Total Globe	13.2 (5.5)	17.3 (1.4)	17.3 (1.4)	17.3 (1.4)	17.4 (1.4)	17.2 (1.3)	17.2 (1.3)	17.2 (1.4)	20.3 (1.4)	20.4 (1.5)	15.2 (1.4)	15.2 (1.4)

[a]Unit is MtN yr^{-1}.

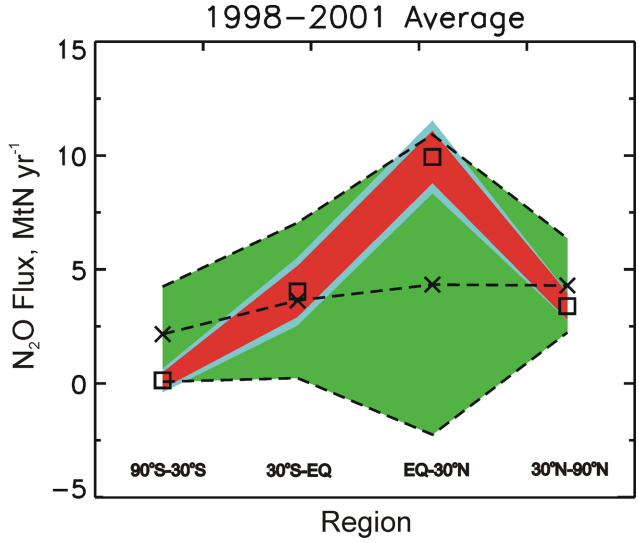

Figure 7. Inverse model results for the four semihemisphere setup, averaged from 1998 through the end of 2001. Prior estimates ±1σ, are shown with crosses and green band. Posterior fluxes are shown as squares ±1σ of the means of cases A–K (red band) and the average of the 1σ a posteriori error from cases A–K (blue band).

the natural terrestrial flux into our total inferred terrestrial flux. Interestingly, the cases with scaled priors (C and D) had the same ocean/land division of the global flux in the prior and posterior fluxes.

3.2. Four Semihemispherical Regions

[25] Figure 7 shows the a priori flux estimates connected by a dotted line, with ±1σ in green. The a posteriori fluxes are shown for each region as squares. The red error band represents ±1σ of the central estimates of cases A–K, while the blue error band is the average of the a posteriori uncertainties (standard deviations) from the inversions A–K. Averaged from 1998–2001, the inferred flux for the 90°S–30°S semihemisphere was lower than the a priori estimate, the inferred flux for the equator-to-30°N semihemisphere was higher than the a priori estimate, and the inferred fluxes for the 30°S-to-equator and 30°N–90°N semihemispheres were close to the a priori estimate (Figure 7 and Table 4a, which includes the a priori flux from case A for reference). In general, the variation of the central a posteriori estimates between model setups is less than the a posteriori uncertainty in the inverse modeling. This result suggests that our inferred flux is not very sensitive to the various assumptions we have made in cases A–K. The (1σ) uncertainty for all of the semihemispheres decreased substantially relative to the a priori uncertainty: a posteriori uncertainties (1σ) were about 24%, 42%, 24%, and 29% of the a priori uncertainties for 90°S–30°S, 30°S-to-equator, equator-to-30°N, and 30°N–90°N regions, respectively. There was some indication, then, that the 30°S-to-equator region was not as well sampled as the others.

[26] In part, the discrepancies between a priori and a posteriori fluxes are due to the difference between the global total a priori and a posteriori fluxes as described above. However, the relative contributions of the different semihemispherical fluxes to the global total were also different from the a priori values and from the results of *Prinn et al.* [1990] (Table 5). On the basis of the central values of the flux estimates, it appears that the relative contributions of the 30°S–90°S and 30°N–90°N semihemispheres were smaller than in the *Prinn et al.* [1990] paper, the equator-to-30°N contribution was substantially higher, and the 30°S-to-equator contribution was similar. As discussed below, it is possible that the differences between this study and the *Prinn et al.* [1990] study are due in part to differences in model transport and measurement network configuration. The range of the *Prinn et al.* [1990] estimates in Table 5 reflects the range of results from different sensitivity runs; the range from this study is the range across the different cases in Table 4a of the ratio of inferred regional flux divided by the inferred global total.

3.3. TransCom3 Super Regions: Multiyear Averages

[27] The a posteriori Tropical Land and Tropical Ocean fluxes from 1998–2001 were higher than the prior estimates (Figure 8 and Table 4b) while the Southern Oceans flux was lower than the prior estimate. To some degree, these shifts occurred because the inversion allocated the difference between the global total a posteriori and a priori fluxes to the tropics as was the case for the semihemispherical basis regions. This result is not surprising, given the relatively large uncertainty of the prior flux for the tropical regions. The error reduction for the Southern Oceans region was substantial, suggesting good sampling of that region by the measurement network. However, the low flux inferred for the Southern Oceans region does not agree with the results of the *Nevison* [1994] study which are part of the GEIA inventory and thus served as our a priori flux estimate. The highest a posteriori flux from this aggregated region (case H) was only 1.0 MtN yr^{-1}, while the a priori value was 1.7 MtN yr^{-1}. This low Southern Ocean result was insensitive to the different assumptions made for the 11 scenarios considered in the study. Uncertainty reduction, calculated here as the ratio of a posteriori to a priori standard deviation, was as follows: Northern Land (50%), Tropical Land (76%), Southern Land (68%), Northern Oceans (70%), Tropical Oceans (60%), and Southern Oceans (35%). Thus, even for these highly aggregated regions, there are large areas of the globe that do not have sufficiently dense sampling to

Table 5. Percent Relative Contribution of Four Semihemisphere Basis Regions to the Global Flux

Study	90°S–30°S	30°S to Equator	Equator to 30°N	30°N–90°N
Prinn et al. [1990]	11–15	20–29	32–39	22–34
GEIA inventory	15	25	30	30
This study	0–4	16–32	50–64	16–23

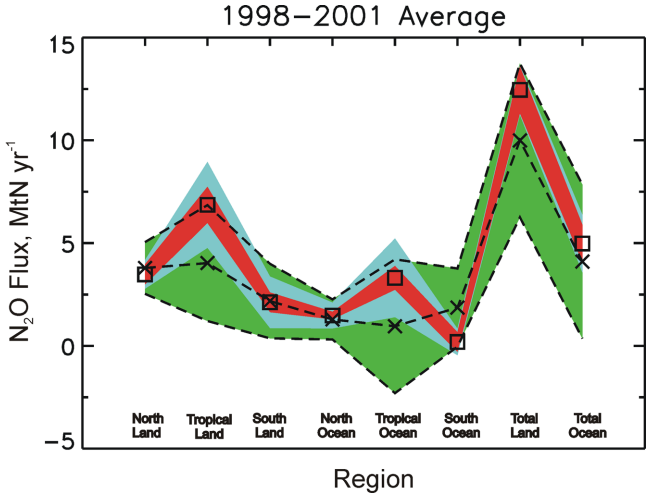

Figure 8. Same as Figure 6, but for the six TransCom3 super regions as well as the global land and ocean totals.

radically reduce the flux uncertainty. Even with good coverage by the sampling network, the error reduction will be limited by the rather low signal-to-noise ratio of the N_2O spatial and temporal patterns. The Northern Oceans result is somewhat surprising, given the density of sampling stations in the temperate and high latitude Northern Hemisphere oceans. It appears, though, that the low level of error reduction is due in large part to an initially low uncertainty on the prior flux (1.0 MtN yr^{-1}).

4. Discussion

[28] Two main results appear to be robust across the different model setups we have tested in this study: (1) N_2O flux from the 90°S–30°S and Southern Oceans super region lower than the prior estimate and (2) high N_2O flux from the equator-to-30°N and Tropical Land and Tropical Ocean super regions relative to the prior estimate. We do not argue that the Tropical Land and Tropical Ocean fluxes can be uniquely determined, because sampling is sparse in those regions. Rather, we would suggest that tropical emissions in general are high relative to the prior (though this difference is less extreme in cases C and D, which use scaled priors). These patterns hold true whether fluxes are distributed evenly across basis regions, or patterned like the GEIA fluxes. They also hold true regardless of the different stratospheric lifetimes assumed, and the treatment of how the stratospheric loss is mixed down to the troposphere. We have confidence that these patterns are not the result of an artifact in the data, given the good agreement with the AGAGE measurements at four widely spread sites. It is conceivable that the slightly larger latitudinal gradient found for the NOAA/ESRL GMD data versus the AGAGE data when comparing Barbados and Cape Grim could influence the contribution inferred for the equator-to-30°N region (Figure 4) relative to the prior estimate. It is also possible that some other model setup could be found that would result in a different pattern; however, to raise the contribution from the 90°S–30°S, it would probably have to include a larger fraction of extratropical stratosphere-troposphere exchange occurring in the Southern Hemisphere. Since we have only investigated the behavior of one transport model, TM3 and one set of analyzed winds, it is valid to ask whether these choices could somehow be biasing the results [*Bousquet et al.*, 1996], for example via the time constant for interhemispheric exchange. We encourage global inverse modeling studies of N_2O with other transport models for comparison. It is also interesting to note that in a model transport intercomparison study using SF_6 [*Denning et al.*, 1999], TM3 had one of the slower exchange times between the 11 models being compared. In the inversion, this slow transport time would have the effect of lowering the ratio of Northern Hemisphere to Southern Hemisphere fluxes, since the Northern Hemisphere fluxes would be slower to mix into the Southern Hemisphere (building up the interhemispheric gradient). Thus the interhemispheric exchange time is unlikely to explain why our inferred ratio of the NH to SH source is at the upper end of previous results. Part of the reason for the relatively high ratio is that our model setup using response functions cause more impact of STE on the Northern Hemisphere, such that Northern Hemisphere fluxes must compensate to give the observed latitudinal gradient. However, even the CLAES-constrained case gave a ratio near the upper end of previous estimates. The high NH/SH ratio may also be due in part to a high interhemispheric difference (IHD) in the data. The IHD, calculated as the average of Mace Head and Barbados minus the average of Cape Grim and Samoa (as in the work of *Prinn et al.* [1990]), was approximately 0.85 (AGAGE) to 1.0 (NOAA/ESRL GMD) ppb averaged from 1998–2001 (Figure 4), exceeding the 1978–1988 average of 0.75 ppb of the *Prinn et al.* [1990] study.

[29] When comparing our results to the results of *Prinn et al.* [1990], we note that there are many differences between the two studies. The transport models, treatment of the stratosphere, inversion technique, and measurement networks all differ. To make a completely robust comparison between the N_2O budgets of the 1980s and the mid-1990s it would be necessary to remove these differences. If the equator-to-30°N region were in fact contributing a greater fraction of the global flux than 2 decades earlier, what could be the cause? One reason could be that nitrogen fertilizer application in Asia has dramatically increased over the past 3 decades. According to the International Fertilizer Industry Association, application of inorganic fertilizer increased in that region by almost 16 MtN yr^{-1} (an increase of about 60%) between 1985 and 1995 (calculated by adding South Asia, Northeast and Southeast Asia, and East Asia categories in the table at the IFA web site: http://www.fertilizer.org/ifa/statistics/indicators/tablen.asp). However, the default IPCC assumption is that only 1.25 ± 1% of applied N fertilizer is directly converted to N_2O, with an additional factor of 0.75% to account for indirect emissions from N that had leached or run off from fields [*Mosier et al.*, 1998]. The corresponding additional emissions from increased fertilizer application would only be about 0.3 MtN yr^{-1}. However, the N_2O yield values are representative of temperate zone measurements, and may not be valid for tropical

ecosystems [*Veldkamp et al.*, 1998]. For example, the fraction of applied fertilizer N lost as N_2O in tropical climates, while varying with soil moisture at the time of fertilization, has been measured to be as high as 20% [*Keller and Matson*, 1994; *Veldkamp et al.*, 1998]. Tropical deforestation (implicated as a major contribution by *Prinn et al.* [1990]) also continued during the 1990s, at the average rate of about 1.5×10^5 km^2 yr^{-1} [*Braatz*, 2001]. Several studies have measured higher N_2O emissions coming from pastures versus undisturbed forest [e.g., *Luizão et al.*, 1989; *Keller et al.*, 1993]. Applying Luizão's best estimate of this difference (380 kgN km^{-2} yr^{-1}) to the approximately 1.5×10^6 km^2 of tropical forest cleared between 1985 and 1995, we calculate a flux increase of about 0.6 MtN yr^{-1}. This figure is an upper estimate, since some of the pastures existing in the 1980s have reverted back to forest and pasture N_2O emissions generally decline after a decade [*Keller et al.*, 1993], offsetting the increased emissions from new clearing.

[30] The low Southern Oceans flux may be consistent with more recent estimates of the flux from that region. The combination of N_2O partial pressure information and air-sea gas exchange model used by *Nevison et al.* [1995], result in a relatively high flux for the Southern Ocean (in fact the Southern Oceans were predicted to have the largest contribution to the ocean total). However, that study and *Suntharalingam et al.* [2000] discuss the still large uncertainties in air-sea gas exchange coefficients and the use of data sets with incomplete spatial and temporal coverage in important production regions. A more recent study of the subsurface production of N_2O [*Nevison et al.*, 2003] suggests that only about 15% of gross global oceanic N_2O is produced south of 30°S. If ventilation of N_2O from this region were limited to N_2O produced in this region and denitrification losses were zero, this would be equivalent to a flux of 0.6–1.2 MtN yr^{-1} for the range of global production quoted in that study. If oceans represent approximately one third of the global total flux, this Southern Ocean flux would correspond to ~5% of the global total, close to the inverse modeling results (Table 5). For that result to be consistent with *Nevison et al.* [1995], where approximately one third of the global flux is contributed by the Southern Ocean, a large amount of N_2O would have to be exported from the tropics and ventilated to the atmosphere. This export term and the resulting ventilation are uncertain [*Suntharalingam et al.*, 2000; *Nevison et al.*, 2003]. Most recently, a study combining ocean modeling and atmospheric measurements [*Nevison et al.*, 2005] placed the Southern Ocean flux at about 0.9 MtN yr^{-1}, roughly half the GEIA estimate.

[31] One important consideration in inverse modeling is whether the inversion actual improves the agreement between measured and modeled concentrations. This agreement can be diagnosed by examining histograms of the difference between "observations," which are the data adjusted for the assumed effects of the stratospheric sink, and the modeled concentrations for all 1695 measurement months using the a posteriori fluxes. The black solid line (Figure 9) uses the GEIA source from case A for the comparison, multiplied by the matrix of Green's functions

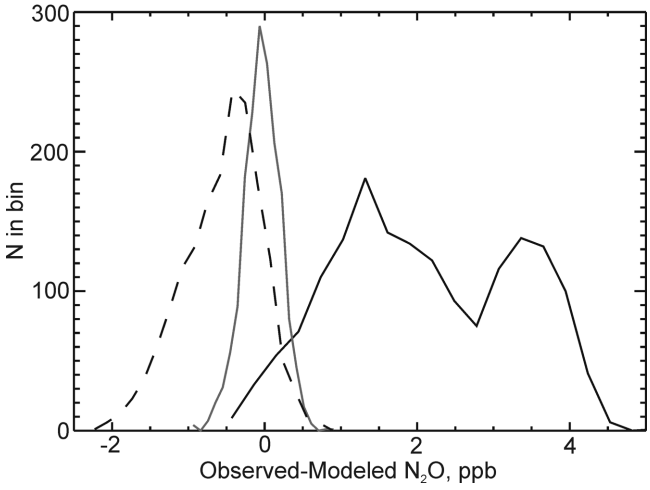

Figure 9. Histograms of the difference between "observed" and modeled N_2O for case A. The "observed" N_2O have been corrected for the stratospheric influence on the measurements. The solid black line represents the observations minus the concentrations that would result from running the GEIA prior flux forward in TM3. The dashed black line is the observations minus the concentrations that would result from running the GEIA source scaled by 1.36 (the prior used in case C) forward. The gray curve centered on zero represents the observations minus the modeled concentrations resulting from the inferred a posteriori fluxes from case A.

to generate concentration data (using TransCom3 super regions for the basis regions, and fluxes patterned like the GEIA source). It is not surprising that the agreement is poor at all sites, because the total source is insufficient to match the stratospheric sink plus the atmospheric accumulation, when assuming a lifetime of 122 years. The gray line uses the a posteriori fluxes from case A to generate pseudo-observations. The differences from the observations are normally distributed around zero, with a standard deviation equal to the value used in the matrix of model-data mismatch values. The most interesting comparison is shown by the black dashed line, which uses the GEIA source scaled by 1.36 (the a priori source for cases C and D) to generate concentrations. The agreement is much better, because the global total source is now consistent with the budget assuming the 122-year lifetime. However, there is a long tail of negative values which represent the modeled N_2O being higher than the "observations." These points mainly represent measurement sites at high northern and southern latitudes. Accordingly, the inverse model has lowered the fluxes in these areas. The agreement is actually quite good using the scaled prior for subtropical and temperate latitudes in both hemispheres. Unfortunately, there are very few sites in the tropics to compare on a site by site basis. Christmas Island observations are higher than the modeled values produced by the scaled prior; however, sites like Seychelles, Guam, and Ascension Island agree very well for most of the record. This agreement makes sense, since the scaled priors for the tropics are fairly close

to the a posteriori estimates. Apparently in case C, the inverse model is shifting the flux from the Northern Land and Southern Oceans super regions to improve the fit there, and adding it to the tropics, where there is less of an observational constraint. Christmas Island appears to play a very important role in constraining tropical fluxes. The same analysis using the four semihemisphere basis regions yields a graph that is basically identical to Figure 9.

5. Conclusions and Future Work

[32] We have found that the NOAA/ESRL GMD CCGG Cooperative Global Air Sampling Network flask measurements of N_2O were able to reduce the uncertainty of monthly N_2O emissions relative to the a priori uncertainty for four semihemispherical regions and for six TransCom3 super regions. However, we were not able to constrain the fluxes very well at smaller scales, such as the original 22 TransCom3 regions. The results also suggest that emissions have shifted such that the equator-to-30°N region now emits a larger fraction of the global total than in the GEIA inventory and the *Prinn et al.* [1990] study and that the Southern Oceans emit a smaller fraction, though we have included caveats regarding the different transport model, treatment of the stratosphere, inversion technique, and measurement network between this study and the *Prinn et al.* [1990] study.

[33] Presently, uncertainties in the distribution of the N_2O flux within regions and the influence of stratospheric air on surface measurements are both large sources of uncertainty. The flux distribution within regions should become better understood when more regional inversion studies are performed within continents (such as those done by *Ryall et al.* [2001] and *Manning et al.* [2003]), using more continuous measurements. Our knowledge of these patterns and the response of the surface flux to different environmental controlling factors is continuously being improved by tracer studies (such as those by *Wilson et al.* [1997], *Schmidt et al* [2001], and *Conen et al.* [2002]), and by a multitude of local scale flux studies.

[34] When the influence of downwelling stratospheric air on surface N_2O measurements is better constrained, it will be possible to investigate the seasonality in the N_2O fluxes for different regions of the globe. Understanding the influence of STE on surface N_2O measurements is also critical to understanding interannual variability in the fluxes even at a global scale; it has been suggested that interannual variability in STE could strongly influence the growth rate for gases with strong stratospheric sinks [*Schauffler and Daniel*, 1994]. Without understanding this influence, these changes in the growth rate would be erroneously interpreted by inverse modeling as temporal changes in the sources. We concluded that presently it made more sense to focus on the long-term average and large-scale behavior since the seasonal cycle (and possibly interannual variability) is very sensitive to the treatment of the stratospheric sink in the model, and our treatment of this effect is presently rather crude. Thus, even though the inverse model can match the atmospheric record at any of the 48 sites to within a few tenths of a ppb in any given month (our inferred model-data mismatch), it is likely that errors in our treatment of the stratospheric sink are being aliased into the seasonal cycle (and possibly interannual variability) of our inferred sources. It may be possible at certain sites to use other tracers of stratospheric influence at the surface such as the $^{10}Be/^{7}Be$ ratio [e.g., *Dibb et al.*, 1994; *Rehfeld and Heimann*, 1995] or CFCs [*Nevison et al.*, 2004, 2005] to help constrain this effect. In addition, vertical profiles could possibly be used in the future to help constrain an inverse model that also solves for the stratospheric loss term in a high-resolution 3D CTM, using the sort of response functions we have employed in this study (analogous to the approach of *Prinn et al.* [1990], using their 12-box model).

[35] **Acknowledgments.** The authors would like to thank all of the collaborators in the NOAA/ESRL GMD CCGG Cooperative Global Air Sampling Network; Martin Heimann (Max Planck Institute for Biogeochemistry) for providing the TM3 code and input wind fields; James Randerson (UC Irvine), William Randel (NCAR), Karen Rosenlof (NOAA), Doug Kinnison, and Cynthia Nevison (NCAR) for helpful conversations about the effect of stratosphere-troposphere exchange on surface measurements of N_2O; Lex Bouwman (RIVM, Netherlands), Changsheng Li (UNH), and Steven Frolking (UNH) their perspectives on terrestrial N_2O fluxes; James Elkins (NOAA) for conversations about N_2O seasonal cycle; and John B. Miller (NOAA) for comments on an earlier draft of the paper and help with statistical and graphical analyses. Finally, we would like to thank two anonymous reviewers for their insightful comments.

References

Appenzeller, C., J. R. Holton, and K. H. Rosenlof (1996), Seasonal variation of mass transport across the tropopause, *J. Geophys. Res.*, *101*(D10), 15,071–15,078.

Battle, M., et al. (1996), Atmospheric gas concentrations over the past century measured in air from firn at the South Pole, *Nature*, *383*(6597), 231–235.

Blackmer, A. M., and J. M. Bremner (1976), Potential of soil as a sink for atmospheric nitrous oxide, *Geophys. Res. Lett.*, *3*, 739–742.

Bousquet, P., P. Ciais, P. Monfray, Y. Balkanski, M. Ramonet, and P. P. Tans (1996), Influence of two different atmospheric transport models on inferring sources and sinks of atmospheric CO_2, *Tellus, Ser. B*, *48*, 568–582.

Bousquet, P., P. Peylin, P. Ciais, C. Le Quere, P. Friedlingstein, and P. P. Tans (2000), Regional changes in carbon dioxide fluxes of land and ocean since 1980, *Science*, *290*, 1342–1346.

Bouwman, A. F., and J. A. Taylor (1996), Testing high-resolution nitrous oxide emission estimates against observations using an atmospheric transport model, *Global Biogeochem. Cycles*, *10*(2), 307–318.

Bouwman, A. F., I. Fung, E. Matthews, and J. John (1993), Global analysis of the potential for N_2O production in natural soils, *Global Biogeochem. Cycles*, *7*(3), 557–598.

Bouwman, A. F., K. W. Van der Hoek, and J. G. J. Olivier (1995), Uncertainties in the global source distribution of nitrous oxide, *J. Geophys. Res.*, *100*(D2), 2785–2800.

Braatz, S. M. (Ed.) (2001), *State of the World's Forests 2001*, U.N. Food and Agric. Org., Rome.

Brice, K. A., et al. (1977), Important ground surface sink for atmospheric nitrous-oxide, *Nature*, *268*(5616), 127–129.

Brown, M. K. M. (1993), Deduction of emissions of sources gases using an objective inversion algorithm and a chemical transport model, *J. Geophys. Res.*, *98*(D7), 12,639–12,660.

Brown, M. (1995), The singular value decomposition method applied to the deduction of the emissions and the isotopic composition of atmospheric methane, *J. Geophys. Res.*, *100*(D6), 11,425–11,446.

Butler, J. H., J. W. Elkins, T. M. Thompson, and K. B. Egan (1989), Tropospheric and dissolved N_2O of the West Pacific and East Indian oceans during the El Niño–Southern Oscillation event of 1987, *J. Geophys. Res.*, *94*(D12), 14,865–14,877.

Castro, M. S., P. A. Steudler, J. M. Melillo, J. D. Aber, and S. Millham (1992), Exchange of N_2O and CH_4 between the atmosphere and soils in spruce-fir forests in the northeastern United States, *Biogeochemistry*, *18*(3), 119–135.

Cicerone, R. J. (1989), Analysis of sources and sinks of atmospheric nitrous oxide (N_2O), *J. Geophys. Res.*, *94*(D15), 18,265–18,271.

Cohen, Y. (1978), Consumption of dissolved nitrous-oxide in an anoxic basin, Saanich Inlet, British Columbia, *Nature*, *272*(5650), 235–237.

Conen, F., A. Neftel, M. Schmid, and B. E. Lehmann (2002), $N_2O/^{222}Rn$–soil flux calibration in the stable nocturnal surface layer, *Geophys. Res. Lett.*, *29*(2), 1025, doi:10.1029/2001GL013429.

Crutzen, P. J. (1974), Estimates of possible variations in total ozone due to natural causes and human activities, *Ambio*, *3*, 201–210.

Denning, A. S., et al. (1999), Three-dimensional transport and concentration of SF_6 A model intercomparison study (TransCom 2), *Tellus, Ser. B*, *51*, 277–297.

Dibb, J. E., L. D. Meeker, R. C. Finkel, J. R. Southon, M. W. Caffee, and L. A. Barrie (1994), Estimation of stratospheric input to the Arctic troposphere: ^{7}Be and ^{10}Be in aerosols at Alert, Canada, *J. Geophys. Res.*, *99*(D6), 12,855–12,864.

Dlugokencky, E. J., L. P. Steele, P. M. Lang, and K. A. Masarie (1994), The growth rate and distribution of atmospheric methane, *J. Geophys. Res.*, *99*(D8), 17,021–17,044.

Donoso, L., R. Santana, and E. Sanhueza (1993), Seasonal variation of N_2O fluxes at a tropical savannah site: Soil consumption of N_2O during the dry season, *Geophys. Res. Lett.*, *20*, 1379–1382.

Elkins, J. W., S. C. Wofsy, M. B. McElroy, C. E. Kolb, and W. A. Kaplan (1978), Aquatic sources and sinks for nitrous oxide, *Nature*, *275*(5681), 602–606.

Enting, I. G. (2002), *Inverse Problems in Atmospheric Constituent Transport*, Cambridge Univ. Press, New York.

Enting, I. G., C. M. Trudinger, and R. J. Francey (1995), A synthesis inversion of the concentration and $\delta^{13}C$ of atmospheric CO_2, *Tellus, Ser. B*, *48*, 35–52.

Fan, S.-M., M. Gloor, J. Mahlman, S. Pacala, J. Sarmiento, T. Takahashi, and P. Tans (1998), A large terrestrial carbon sink in North America implied by atmospheric and ocean CO_2 data and models, *Science*, *282*, 442–446.

Flückiger, J., E. Monnin, B. Stauffer, J. Schwander, T. F. Stocker, J. Chappellaz, D. Raynaud, and J. Barnola (2002), High-resolution Holocene N_2O ice core record and its relationship with CH_4 and CO_2, *Global Biogeochem. Cycles*, *16*(1), 1010, doi:10.1029/2001GB001417.

Gettelman, A., and A. H. Sobel (2000), Direct diagnoses of stratosphere-troposphere exchange, *J. Atmos. Sci.*, *57*(1), 3–16.

Gettelman, A., J. R. Holton, and K. H. Rosenlof (1997), Mass fluxes of O_3, CH_4, N_2O and CF_2Cl_2 in the lower stratosphere calculated from observational data, *J. Geophys. Res.*, *102*(D15), 19,149–19,159.

Gurney, K. R., et al. (2002), Towards robust regional estimates of CO_2 sources and sinks using atmospheric transport models, *Nature*, *415*(6872), 626–630.

Hall, B. D., et al. (2002), Halocarbons and other atmospheric trace species, in *Climate Monitoring and Diagnostics Laboratory*, edited by D. B. King et al., *Summary Rep. 26 2000–2001*, pp. 106–135, U.S. Dep. of Commer., Boulder, Colo.

Hao, W., S. Wofsy, M. B. McElory, J. M. Beer, and M. A. Togan (1987), Sources of atmospheric nitrous oxide from combustion, *J. Geophys. Res.*, *92*(D3), 3098–3104.

Hartley, D., and R. Prinn (1993), Feasibility of determining surface emissions of trace gases using an inverse method in a three-dimensional chemical transport model, *J. Geophys. Res.*, *98*(D3), 5183–5197.

Heimann, M. (1995), The global atmospheric tracer model TM2, *Tech. Rep. 10*, Klimarechenzentrum, Max-Planck-Inst. für Meteorol., Berlin.

Heimann, M., and S. Körner (2003), The Global Atmospheric Tracer Model TM3: Model description and user's manual release 3.8a, *Tech. Rep. 5*, Max Planck Inst. für Biogeochem., Jena, Germany.

Hein, R., P. J. Crutzen, and M. Heimann (1997), An inverse modeling approach to investigate the global atmospheric methane cycle, *Global Biogeochem. Cycles*, *11*(1), 43–76.

Houweling, S., T. Kaminski, F. Dentener, J. Lelieveld, and M. Heimann (1999), Inverse modeling of methane sources and sinks using the adjoint of a global transport model, *J. Geophys. Res.*, *104*(D21), 26,137–26,160.

Kaminski, T., M. Heimann, and R. Giering (1999), A coarse grid three-dimensional global inverse model of the atmospheric transport: 2. Inversion of the transport of CO_2 in the 1980s, *J. Geophys. Res.*, *104*(D21), 18,535–18,553.

Keller, M., and P. A. Matson (1994), Biosphere-atmosphere exchange of trace gases in the tropics: Evaluating the effects of land use change, in *Global Atmospheric-Biospheric Chemistry*, edited by R. Prinn, pp. 103–117, Springer, New York.

Keller, M., E. Veldkamp, A. M. Weitz, and W. A. Reiners (1993), Effect of pasture age on soil trace-gas emissions from a deforested area of Costa Rica, *Nature*, *365*(6443), 244–246.

Khalil, M. A. K., and R. A. Rasmussen (1992), The global sources of nitrous oxide, *J. Geophys. Res.*, *97*(D13), 14,651–14,660.

Kroeze, C., A. Mosier, and L. Bouwman (1999), Closing the global N_2O budget: A retrospective analysis 1500–1994, *Global Biogeochem. Cycles*, *13*(1), 1–9.

Kumer, J. B., J. L. Mergenthaler, and A. E. Roche (1993), CLAES CH_4, N_2O, and CCl_2F_2 (F12) global data, *Geophys. Res. Lett.*, *20*, 1239–1242.

Law, R., and I. Simmonds (1996), The sensitivity of deduced CO_2 sources and sinks to variations in transport and imposed surface concentrations, *Tellus, Ser. B*, *48*, 613–625.

Levy, H., II, J. D. Mahlman, and W. J. Moxim (1982), Tropospheric N_2O variability, *J. Geophys. Res.*, *87*(C4), 3061–3080.

Liao, T., C. D. Camp, and Y. L. Yung (2004), The seasonal cycle of N_2O, *Geophys. Res. Lett.*, *31*, L17108, doi:10.1029/2004GL020345.

Luizão, F., P. Matson, G. Livingston, R. Luizao, and P. Vitousek (1989), Nitrous oxide flux following tropical land clearing, *Global Biogeochem. Cycles*, *3*(3), 281–285.

Machida, T., T. Nakazawa, Y. Fujii, S. Aoki, and O. Watanabe (1995), Increase in the atmospheric nitrous-oxide concentration during the last 250 years, *Geophys. Res. Lett.*, *22*, 2921–2924.

Manning, A. J., D. B. Ryall, R. G. Derwent, P. G. Simmonds, and S. O'Doherty (2003), Estimating European emissions of ozone-depleting and greenhouse gases using observations and a modeling back-attribution technique, *J. Geophys. Res.*, *108*(D14), 4405, doi:10.1029/2002JD002312.

Michalak, A. M., A. I. Hirsch, L. Bruhwiler, K. R. Gurney, W. Peters, and P. P. Tans (2005), Maximum likelihood estimation of covariance parameters for Bayesian atmospheric trace gas surface flux inversions, *J. Geophys. Res.*, *110*, D24107, doi:10.1029/2005JD005970.

Minschwaner, K., R. Salawich, and M. McElroy (1993), Absorption of solar radiation by O_2: Implications for O_3 and lifetimes of N_2O, $CFCl_3$, and CF_2Cl_2, *J. Geophys. Res.*, *98*(D6), 10,543–10,561.

Morgan, C. G., M. Allen, M. C. Liang, R. L. Shia, G. A. Blake, and Y. L. Yung (2004), Isotopic fractionation of nitrous oxide in the stratosphere: Comparison between model and observations, *J. Geophys. Res.*, *109*, D04305, doi:10.1029/2003JD003402.

Mosier, A., C. Kroeze, C. Nevison, O. Oenema, S. Seitzinger, and O. van Cleemput (1998), Closing the global N_2O budget: Nitrous oxide emissions through the agricultural nitrogen cycle, *Nutr. Cycl. Agroecosyst.*, *52*, 223–245.

Mulquiney, J. E., and J. A. Norton (1998), A new inverse method for trace gas flux estimation: 1. State-space model identification and constraints, *J. Geophys. Res.*, *103*(D1), 1417–1427.

Mulquiney, J. E., J. A. Taylor, A. J. Jakeman, J. P. Norton, and R. G. Prinn (1998), A new inverse method for trace gas flux estimation: 2. Application to tropospheric CFCl3 fluxes, *J. Geophys. Res.*, *103*(D1), 1429–1442.

Muzio, L. J., and J. C. Kramlich (1988), An artifact in the measurement of N_2O from combustion sources, *Geophys. Res. Lett.*, *15*, 1369–1372.

Nevison, C. (1994), A model analysis of the spatial distribution and temporal trends of nitrous oxide sources and sinks, Ph.D. thesis, Stanford Univ., Stanford, Calif.

Nevison, C. D., and E. Holland (1997), A re-examination of the impact of anthropogenically fixed nitrogen on atmospheric N_2O and the stratospheric O_3 layer, *J. Geophys. Res.*, *102*(D21), 25,519–25,536.

Nevison, C. D., R. F. Weiss, and D. J. Erickson III (1995), Global oceanic emissions of nitrous oxide, *J. Geophys. Res.*, *100*(C8), 15,809–15,820.

Nevison, C. D., G. Esser, and E. A. Holland (1996), A global model of changing N_2O emissions from natural and perturbed soils, *Clim. Change*, *32*(3), 327–378.

Nevison, C. D., J. H. Butler, and J. W. Elkins (2003), Global distribution of N_2O and the ΔN_2O-AOU yield in the subsurface ocean, *Global Biogeochem. Cycles*, *17*(4), 1119, doi:10.1029/2003GB002068.

Nevison, C. D., D. E. Kinnison, and R. F. Weiss (2004), Stratospheric influences on the tropospheric seasonal cycles of nitrous oxide and chlorofluorocarbons, *Geophys. Res. Lett.*, *31*, L20103, doi:10.1029/2004GL020398.

Nevison, C. D., R. F. Keeling, R. F. Weiss, B. N. Popp, X. Jin, L. W. Porter, and P. G. Hess (2005), Southern Ocean ventilation inferred from seasonal cycles of atmospheric N_2O and O_2/N_2 at Cape Grim, Tasmania, *Tellus, Ser. B*, *5*, 218, doi:10.1111/j.1600-0889.2005.00143.x.

Pierotti, D., and R. A. Rasmussen (1976), Combustion as a source of nitrous oxide in the atmosphere, *Geophys. Res. Lett.*, *3*, 265–267.

Plumb, R. A., and X. Zheng (1996), Source determination from trace gas observations: An orthogonal function approach and results for long-lived gases with surface sources, *J. Geophys. Res.*, *101*(D13), 18,569–18,585.

Potter, C. S., P. A. Matson, P. M. Vitousek, and E. A. Davidson (1996), Process modeling of controls on nitrogen trace gas emissions from soils worldwide, *J. Geophys. Res.*, *101*(D1), 1361–1377.

Prather, M., and D. Ehhalt (2001), Atmospheric chemistry and greenhouse gases, in *Climate Change 2001: The Scientific Basis*, edited by J. T. Houghton et al., pp. 239–287, Cambridge Univ. Press, New York.

Prinn, R., D. Cunnold, R. Rasmussen, P. Simmonds, F. Alyea, A. Crawford, P. Fraser, and R. Rosen (1990), Atmospheric emissions and trends of nitrous oxide deduced from 10 years of ALE-GAGE data, *J. Geophys. Res.*, *95*(D11), 18,369–18,385.

Prinn, R. G., et al. (1998), Long-lived ozone-related compounds in *Scientific Assessment of Ozone Depletion: 1998*, edited by C. A. Ennis, pp. I-1–I-54, World Meteorol. Org., Geneva.

Prinn, R. G., et al. (2000), A history of chemically and radiatively important gases in air deduced from ALE/GAGE/AGAGE, *J. Geophys. Res.*, *105*(D14), 17,751–17,792.

Rahn, T., and M. Wahlen (2000), A reassessment of the global isotopic budget of atmospheric nitrous oxide, *Global Biogeochem. Cycles*, *14*(2), 537–543.

Randel, W. J., B. A. Boville, J. C. Gille, P. L. Bailey, S. T. Massie, J. B. Kumer, J. L. Mergenthaler, and A. E. Roche (1994), Simulation of stratospheric N_2O in the NCAR CCM2: Comparison with CLAES data and global budget analyses, *J. Atmos. Sci.*, *51*(20), 2834–2845.

Randerson, J. T., I. G. Enting, E. A. G. Schuur, K. Caldeira, and I. Y. Fung (2002), Seasonal and latitudinal variability of troposphere $\Delta^{14}CO_2$: Post bomb contributions from fossil fuels, oceans, the stratosphere, and the terrestrial biosphere, *Global Biogeochem. Cycles*, *16*(4), 1112, doi:10.1029/2002GB001876.

Rehfeld, S., and M. Heimann (1995), Three-dimensional atmospheric transport simulation of the radioactive tracers ^{210}Pb, ^{7}Be, ^{10}Be, and ^{90}Sr, *J. Geophys. Res.*, *100*(D12), 26,141–26,161.

Röckmann, T., J. Kaiser, and C. A. M. Brenninkmeijer (2002), The isotopic fingerprint of the pre-industrial and the anthropogenic N_2O source, *Atmos. Chem. Phys. Discuss.*, *2*, 2021–2043.

Rödenbeck, C., S. Houweling, M. Gloor, and M. Heimann (2003), CO_2 flux history 1982–2001 inferred from atmospheric data using a global inversion of atmospheric transport, *Atmos. Chem. Phys. Discuss.*, *3*, 2575–2659.

Ryall, D. B., R. G. Derwent, P. G. Simmonds, and S. J. O'Doherty (2001), Estimating source regions of European emissions of trace gases from observations at Mace Head, *Atmos. Environ.*, *35*, 2507–2523.

Ryden, J. C. (1981), N_2O exchange between a grassland soil and the atmosphere, *Nature*, *292*(5820), 235–237.

Schauffler, S. M., and J. S. Daniel (1994), On the effects of stratospheric circulation changes on trace gas trends, *J. Geophys. Res.*, *99*(D12), 25,747–25,754.

Schiller, C. L., and D. R. Hastie (1994), Exchange of nitrous oxide within the Hudson Bay lowland, *J. Geophys. Res.*, *99*(D1), 1573–1588.

Schmidt, M., H. Glatzel-Mattheier, H. Sartorius, D. E. Worthy, and I. Levin (2001), Western European N_2O emissions: A top-down approach based on atmospheric observations, *J. Geophys. Res.*, *106*(D6), 5507–5516.

Schoberl, M. R. (2004), Extratropical stratosphere-troposphere mass exchange, *J. Geophys. Res.*, *109*, D13303, doi:10.1029/2004JD004525.

Suntharalingam, P., J. L. Sarmiento, and J. R. Toggweiler (2000), Global significance of nitrous-oxide production and transport from oceanic low-oxygen zones: A modeling study, *Global Biogeochem. Cycles*, *14*(4), 1353–1370.

Tans, P. P., I. Y. Fung, and T. Takahashi (1990), Observational constraints on the global atmospheric CO_2 budget, *Science*, *247*, 1431–1438.

Veldkamp, E., M. Keller, and M. Nuñez (1998), Effects of pasture management on N_2O and NO emissions from soils in the humid tropics of Costa Rica, *Global Biogeochem. Cycles*, *12*(1), 71–80.

Volk, C. M., J. W. Elkins, D. W. Fahey, G. S. Dutton, J. M. Gilligan, M. Loewenstein, J. R. Podolske, K. R. Chan, and M. R. Gunson (1997), Evaluation of source gas lifetimes from stratospheric observations, *J. Geophys. Res.*, *102*(D21), 25,543–25,564.

Weiss, R. F., and H. Craig (1976), Production of nitrous oxide by combustion, *Geophys. Res. Lett.*, *3*, 751–753.

Wilson, S. R., et al. (1997), Nitrous oxide flux estimates from south-east Australia, *J. Atmos. Chem.*, *26*, 169–188.

Zander, R. E., et al. (1994), Monitoring of the atmospheric burdens of CH_4, N_2O, CO, $CHClF_2$ and CF_2Cl_2 above central Europe during the last decade, *Environ. Monit. Assess.*, *31*, 203–209.

L. M. Bruhwiler, E. J. Dlugokencky, A. I. Hirsch, W. Peters, and P. P. Tans, Global Monitoring Division, Earth System Research Laboratory, National Oceanic and Atmospheric Administration, 325 Broadway R/GMD1, Boulder, CO 80305-3328, USA. (adam.hirsch@noaa.gov)

A. M. Michalak, Department of Civil and Environmental Engineering, University of Michigan, Ann Arbor, MI 48109-2125, USA.